

## THE MOSDEF SURVEY: EXCITATION PROPERTIES OF $z \sim 2.3$ STAR-FORMING GALAXIES<sup>1</sup>

ALICE E. SHAPLEY,<sup>2</sup> NAVEEN A. REDDY,<sup>3,4</sup> MARISKA KRIEK,<sup>5</sup> WILLIAM R. FREEMAN,<sup>3</sup> RYAN L. SANDERS,<sup>2</sup> BRIAN SIANA,<sup>3</sup>  
ALISON L. COIL,<sup>6</sup> BAHRAM MOBASHER,<sup>3</sup> IRENE SHIVAEI,<sup>3</sup> SEDONA H. PRICE,<sup>5</sup> & LAURA DE GROOT,<sup>3</sup>

*Draft version March 24, 2018*

### ABSTRACT

We present results on the excitation properties of  $z \sim 2.3$  galaxies using early observations from the MOSFIRE Deep Evolution Field (MOSDEF) Survey. With its coverage of the full suite of strong rest-frame optical emission lines, MOSDEF provides an unprecedented view of the rest-frame optical spectra of a representative sample of distant star-forming galaxies. We investigate the locations of  $z \sim 2.3$  MOSDEF galaxies in multiple emission-line diagnostic diagrams. These include the [OIII] $\lambda 5007$ /H $\beta$  vs. [NII]/H $\alpha$  and [OIII] $\lambda 5007$ /H $\beta$  vs. [SII] $\lambda\lambda 6717, 6731$ /H $\alpha$  “BPT” diagrams, as well as the  $O_{32}$  vs.  $R_{23}$  excitation diagram. We recover the well-known offset in the star-forming sequence of high-redshift galaxies in the [OIII] $\lambda 5007$ /H $\beta$  vs. [NII]/H $\alpha$  BPT diagram relative to Sloan Digital Sky Survey star-forming galaxies. However, the shift for our rest-frame optically selected sample is less significant than for rest-frame-UV selected and emission-line selected galaxies at  $z \sim 2$ . Furthermore, we find that the offset is mass-dependent, only appearing within the low-mass half of the  $z \sim 2.3$  MOSDEF sample, where galaxies are shifted towards higher [NII]/H $\alpha$  at fixed [OIII]/H $\beta$ . Within the [OIII] $\lambda 5007$ /H $\beta$  vs. [SII]/H $\alpha$  and  $O_{32}$  vs.  $R_{23}$  diagrams, we find that  $z \sim 2.3$  galaxies are distributed like local ones, and therefore attribute the shift in the [OIII] $\lambda 5007$ /H $\beta$  vs. [NII]/H $\alpha$  BPT diagram to elevated N/O abundance ratios among lower-mass ( $M_* < 10^{10} M_\odot$ ) high-redshift galaxies. The variation in N/O ratios calls into question the use at high redshift of oxygen abundance indicators based on nitrogen lines, but the apparent invariance with redshift of the excitation sequence in the  $O_{32}$  vs.  $R_{23}$  diagram paves the way for using the combination of  $O_{32}$  and  $R_{23}$  as an unbiased metallicity indicator over a wide range in redshift. This indicator will allow for an accurate characterization of the shape and normalization of the mass-metallicity relationship over more than 10 Gyr.

*Subject headings:* galaxies: evolution — galaxies:high-redshift — galaxies: ISM

### 1. INTRODUCTION

Rest-frame optical emission-line spectra contain a wealth of information about the fundamental properties of galaxies. These include the instantaneous star-formation rate, the degree of nebular dust extinction, the electron density in star-forming regions, the gas-phase chemical abundance, and the nature of the ionizing energy source, be it hot stars, an active galactic nucleus (AGN), or shocks. Accordingly, the nebular emission lines in the spectra of both individual H II regions and the integrated light from galaxies follow well-defined patterns and correlations that reflect the range of underlying physical conditions in star-forming regions and active nuclei. These patterns have been well-traced among the ensemble of the strongest rest-frame optical emission lines, including [OII] $\lambda\lambda 3726, 3729$ , H $\beta$ , [OIII] $\lambda\lambda 4959, 5007$ , H $\alpha$ ,

[NII] $\lambda 6584$ , and [SII] $\lambda\lambda 6717, 6731$ .

Building on earlier work by Baldwin et al. (1981), Veilleux & Osterbrock (1987) proposed three diagnostic emission-line diagrams featuring the following axes: [OIII] $\lambda 5007$ /H $\beta$  vs. [NII] $\lambda 6585$ /H $\alpha$ , [OIII] $\lambda 5007$ /H $\beta$  vs. [SII] $\lambda\lambda 6717, 6731$ /H $\alpha$ , and [OIII] $\lambda 5007$ /H $\beta$  vs. [OI] $\lambda 6300$ /H $\alpha$ , commonly referred to as “BPT” diagrams in reference to the original Baldwin et al. work. These diagrams can be used to distinguish the ionizing mechanism in emission-line galaxies, specifically whether it is from hot stars or an active nucleus. Star-forming galaxies occupy very well-defined loci in these diagnostic diagrams, in particular in the [OIII] $\lambda 5007$ /H $\beta$  vs. [NII] $\lambda 6585$ /H $\alpha$  diagram. As metallicity increases, the sequence of star-forming galaxies in the space of [OIII] $\lambda 5007$ /H $\beta$  vs. [NII] $\lambda 6585$ /H $\alpha$  extends from high values of [OIII] $\lambda 5007$ /H $\beta$  and low [NII] $\lambda 6585$ /H $\alpha$ , and curves down to low [OIII] $\lambda 5007$ /H $\beta$  and high [NII] $\lambda 6585$ /H $\alpha$ . Galaxy stellar mass also increases along the sequence, due to the relationship between stellar mass and gas-phase metallicity in star-forming galaxies (Tremonti et al. 2004). Another diagnostic diagram commonly used to characterize star-forming galaxies is the space of [OIII] $\lambda\lambda 4959, 5007$ /[OII] $\lambda\lambda 3726, 3729$  ( $O_{32}$ ) vs. ([OIII] $\lambda\lambda 4959, 5007$ + [OII] $\lambda\lambda 3726, 3729$ )/H $\beta$  ( $R_{23}$ ). Photoionization models (Ferland et al. 1998; Kewley & Dopita 2002; Dopita et al. 2013) tuned to match the distributions of local galaxies in these diagnostic diagrams have been used to translate observed sets of emission lines into physical quantities such as oxygen

Electronic address: aes@astro.ucla.edu

<sup>1</sup> Based on data obtained at the W.M. Keck Observatory, which is operated as a scientific partnership among the California Institute of Technology, the University of California, and the National Aeronautics and Space Administration, and was made possible by the generous financial support of the W.M. Keck Foundation.

<sup>2</sup> Department of Physics and Astronomy, University of California, Los Angeles, 430 Portola Plaza, Los Angeles, CA 90095, USA

<sup>3</sup> Department of Physics and Astronomy, University of California, Riverside, 900 University Avenue, Riverside, CA, 92521, USA

<sup>4</sup> Alfred P. Sloan Fellow

<sup>5</sup> Astronomy Department, University of California at Berkeley, Berkeley, CA 94720, USA

<sup>6</sup> Center for Astrophysics and Space Sciences, Department of Physics, University of California, San Diego, 9500 Gilman Drive., La Jolla, CA 92093, USA

abundance, ionization parameter (i.e., ratio of ionizing photon to particle density in H II regions), and hardness of the ionizing spectrum.

Over the past 15 years, rest-frame optical measurements have been assembled for galaxies at  $z > 1$  using near-IR spectrographs on large ground-based telescopes, providing a window into distant star-forming regions. Based on typically small samples and incomplete sets of rest-frame optical emission lines (e.g., [NII]/H $\alpha$  in the K-band at  $z \sim 2$ , or H-band at  $z \sim 1.5$ ), we have begun to probe the evolution in galaxy metallicity (e.g., Erb et al. 2006a), dust content (e.g., Domínguez et al. 2013; Price et al. 2014), and H II region physical conditions (e.g., Shirazi et al. 2014).

Intriguingly, early observations of H $\beta$ , [OIII] $\lambda$ 5007, H $\alpha$ , and [NII] $\lambda$ 6584 suggested a systematic offset in the [OIII] $\lambda$ 5007/H $\beta$  vs. [NII] $\lambda$ 6585/H $\alpha$  star-forming sequence of galaxies at  $z > 1$ , relative to that of local galaxies in the Sloan Digital Sky Survey (SDSS) (Shapley et al. 2005; Liu et al. 2008; Erb et al. 2006b). These observations have inspired many different explanations, including evolution with redshift in the typical interstellar pressure, and typical H II-region ionization parameters, electron densities, density structure, and ionizing spectra (Liu et al. 2008; Brinchmann et al. 2008; Kewley et al. 2013; Yeh et al. 2013). Alternatively, the offset has been explained as the contribution by weak, unresolved AGN emission (e.g., Wright et al. 2010). Furthermore, Juneau et al. (2014) have highlighted the importance of accounting for selection effects at high redshift. The BPT offset also raised red flags about inferring oxygen abundances in high-redshift galaxies using locally-calibrated strong-line metallicity indicators (Pettini & Pagel 2004), which are tied to either the ratio of [NII] $\lambda$ 6584/H $\alpha$  (the  $N2$  indicator) or that of ([OIII] $\lambda$ 5007/H $\beta$ )/([NII] $\lambda$ 6584/H $\alpha$ ) (the  $O3N2$  indicator). Indeed, if the high-redshift galaxies follow different patterns from those of local galaxies in the [OIII] $\lambda$ 5007/H $\beta$  vs. [NII] $\lambda$ 6585/H $\alpha$  BPT diagram, it seems likely that a different translation is required between strong-line emission ratios and oxygen abundance (Liu et al. 2008; Newman et al. 2014).

Despite signaling some potentially important physical changes in galaxies at high redshift, the samples used to measure their emission-line excitation properties to date have been small and limited to the [OIII] $\lambda$ 5007/H $\beta$  vs. [NII] $\lambda$ 6585/H $\alpha$  diagnostic diagram. To assemble the full picture, we need a statistical and unbiased sample of galaxies with coverage across multiple diagnostic diagrams. Now with the advent of multi-object near-IR spectrographs on 8 – 10-meter-class telescopes, we are poised to systematically characterize the emission-line patterns among high-redshift galaxies, using the full suite of strong rest-frame optical emission lines spanning in wavelength from [OII] $\lambda$ 3726, 3729 to [SII] $\lambda$ 6717, 6731. The MOSFIRE Deep Evolution Field (MOSDEF) survey provides the ideal dataset for such investigations. When complete, MOSDEF will contain rest-frame optical spectra of  $\sim 1500$  galaxies at  $z \sim 1.4 - 3.8$ , including sensitive observations of all of the relevant strong rest-frame optical emission lines at  $z \sim 1.6 - 2.6$ , and most features over the full redshift range. Furthermore, as MOSDEF is conducted in *Hubble Space Telescope* (HST) legacy fields (Grogin et al. 2011; Koekemoer et al. 2011),

each MOSDEF target has extensive multi-wavelength ancillary data. Therefore, rest-frame optical emission-line properties can be connected with other basic galaxy properties such as stellar mass, star-formation history, and morphology. In this paper, we demonstrate the power of the MOSDEF survey for characterizing the physical properties of star-forming galaxies at  $z \sim 2$ , based on their patterns of rest-frame optical emission lines.

In Section 2, we give a brief overview of the MOSDEF survey, describing our observations, measurements, and sample selection. Section 3 presents our results on the excitation diagrams of  $z \sim 2.3$  MOSDEF galaxies, and how they relate to those in the local universe. In Section 4, we conclude by discussing the implications of the excitation properties of  $z \sim 2.3$  galaxies for abundance ratio variations, and proposing a new oxygen abundance indicator for high-redshift galaxies. Throughout this paper we assume a  $\Lambda$ -CDM cosmology with  $H_0 = 70 \text{ km s}^{-1} \text{ Mpc}^{-1}$ ,  $\Omega_m = 0.3$ , and  $\Omega_\Lambda = 0.7$ .

## 2. OBSERVATIONS AND ANALYSIS

### 2.1. The MOSDEF Survey

Our analysis is based on early observations from the MOSDEF survey. MOSDEF is a four-year project using the MOSFIRE spectrograph (McLean et al. 2012) on the 10 m Keck I telescope to measure the physical properties of galaxies at  $1.4 \leq z \leq 3.8$ . The full details of the MOSDEF survey design, observations, and analysis are described in Kriek et al. (2014). In brief, we target galaxies over 500 square arcminutes in the AEGIS, COSMOS, and GOODS-N extragalactic legacy fields with *Hubble Space Telescope* (HST) imaging coverage from the Cosmic Assembly Near-infrared Deep Extragalactic Legacy Survey (CANDELS; Grogin et al. 2011; Koekemoer et al. 2011) and HST/WFC3 grism spectroscopy from the 3D-HST survey (Brammer et al. 2012). All MOSDEF targets have extensive multi-wavelength ancillary data and robust photometric redshifts, while  $\sim 40\%$  have previously-determined spectroscopic redshifts. MOSDEF targets fall in three redshift intervals ( $1.37 \leq z \leq 1.70$ ,  $2.09 \leq z \leq 2.61$ , and  $2.95 \leq z \leq 3.80$ ), which are dictated by the desire to cover rest-frame optical emission lines within windows of atmospheric transmission, and are selected down to limiting HST/WFC3 F160W magnitudes of 24.0, 24.5, and 25.0, respectively, at  $z \sim 1.5, 2.3$ , and 3.4. When complete, MOSDEF will include rest-frame optical spectra for  $\sim 1500$  galaxies, with roughly half the sample at  $2.09 \leq z \leq 2.61$ , and the other half evenly divided between the other two redshift intervals.

### 2.2. Observations, Reductions, and Analysis

In this paper, we focus on galaxies at  $z \sim 2.3$ , which comprise the bulk of the sample in early MOSDEF observations. For these galaxies, we collected J, H, and K-band spectra, to maximize the set of strong optical emission lines covered at rest-frame 3700 – 7000 Å. The nominal exposure time in each band is 2 hours per filter, corresponding to  $3\sigma$  H $\alpha$  emission-line detections for objects with unobscured star-formation rates of  $\sim 1 M_\odot \text{ yr}^{-1}$ . The data presented here were collected over the course of five observing runs from 2012 December to 2013 May

and include eight MOSFIRE masks.<sup>7</sup> In addition to the main MOSDEF target fields, we obtained a single mask in each of the GOODS-S and UDS fields, due to the lack of field visibility in 2012 December. Each mask had  $\sim 30$   $0''.7$  slits, yielding a resolution of, respectively, 3300 in J, 3650 in H, and 3600 in K. For galaxies at  $z \sim 2.3$ , we typically cover [OII] $\lambda\lambda 3726, 3729$  in the J band, H $\beta$  and [OIII] $\lambda\lambda 4959, 5007$  in the H band, and H $\alpha$ , [NII] $\lambda 6584$ , and [SII] $\lambda\lambda 6717, 6731$  in the K band.

We reduced the data in two dimensions using a custom IDL pipeline (see Kriek et al. 2014, for a full description), yielding both signal and error frames for each slit. One-dimensional signal and error spectra for both primary targets and serendipitous objects falling on each slit were then optimally extracted (Freeman et al., in prep.). The relative spectral response was established with observations of B8 – A1 V telluric standard stars, and tied to an absolute scale by matching the flux density in the spectrum of a reference star on the mask to its broadband photometry. Such reference stars were drawn from the 3D-HST photometric catalogs, with  $H_{AB} \leq 20.5$ . As described in detail in Kriek et al. (2014), this initial calibration was refined for each galaxy based on the predicted amount of differential slit loss relative to the reference star, which is a function of *HST* morphology and seeing. Our careful methodology for flux calibration is required to estimate emission-line ratios spanning multiple filters, with data potentially collected under different seeing conditions in different filters. As a test of this method, we compared the measured spectroscopic flux density and the flux density in the best-fit spectral energy distribution to the multi-wavelength photometric dataset for the sample of objects with detected continuum. The overall agreement between these two sets of flux densities suggests no significant bias in the slit-loss corrected line fluxes, with the assumption that line emission has the same spatial distribution as that of the continuum. This analysis also suggests that the uncertainty from slit loss corrections for line ratios spanning multiple filters is  $\approx 18\%$  (Kriek et al. 2014).

We measured emission-line fluxes with Gaussian line profile fits to the extracted, flux-calibrated one-dimensional spectra. The highest signal-to-noise (S/N) emission line (typically H $\alpha$  or [OIII] $\lambda 5007$ ) was used to obtain an initial estimate of the nebular redshift and FWHM. The corresponding values for all other detected emission lines were constrained to be close to these initial estimates (Kriek et al. 2014). Furthermore, the [OII] and [SII] doublets were each fit as the sum of two Gaussians, while the combination of H $\alpha$  and the [NII] doublet was deblended with three Gaussians. Line-flux uncertainties were estimated through Monte Carlo simulations in which we perturbed the one-dimensional spectra a large number of times according to their error spectra, re-measuring emission lines in each perturbed spectrum, and measuring the standard deviation of the resulting distribution of perturbed fluxes. The MOSFIRE redshift for each galaxy, which is used for our analysis, was estimated from the observed centroid of the high-

est S/N emission line. Balmer emission-line fluxes were corrected for underlying stellar absorption based on the equivalent widths of stellar Balmer features as estimated from the stellar population synthesis model fit to the multi-wavelength spectral energy distribution (SED) of each galaxy (Reddy et al., in prep). Balmer absorption is negligible for H $\alpha$ , but manifests as a median correction of 14, 12, and 6%, for H $\beta$ , respectively, within the [OIII] $\lambda 5007$ /H $\beta$  vs. [NII] $\lambda 6585$ /H $\alpha$ , [OIII] $\lambda 5007$ /H $\beta$  vs. [SII]/H $\alpha$ , and  $O_{32}$  vs.  $R_{23}$  samples described in Section 2.3.

Several key galaxy properties were derived from a combination of our MOSFIRE measurements and existing ancillary data. Nebular extinction,  $E(B - V)_{neb}$ , was estimated based on the stellar-absorption-corrected H $\alpha$ /H $\beta$  ratio, assuming an intrinsic ratio of 2.86 (appropriate for  $T_e = 10,000$  K; Osterbrock 1989) and using the dust-attenuation curve of Cardelli et al. (1989). Star-formation rates (SFRs) were estimated from dust-corrected H $\alpha$  luminosities, using the calibration of Kennicutt (1998) converted to a Chabrier (2003) IMF. Stellar masses ( $M_*$ ) were estimated using the pre-existing multi-wavelength photometry assembled by the 3D-HST team (Skelton et al. 2014), with spectroscopic redshifts fixed by our MOSFIRE measurements. For SED fitting, we used the program FAST (Kriek et al. 2009), assuming the stellar population synthesis models of Conroy et al. (2009) and a Chabrier (2003) IMF. Specific SFRs (sSFRs) were estimated as the ratio between the dust-corrected H $\alpha$  SFRs and stellar masses. Finally,

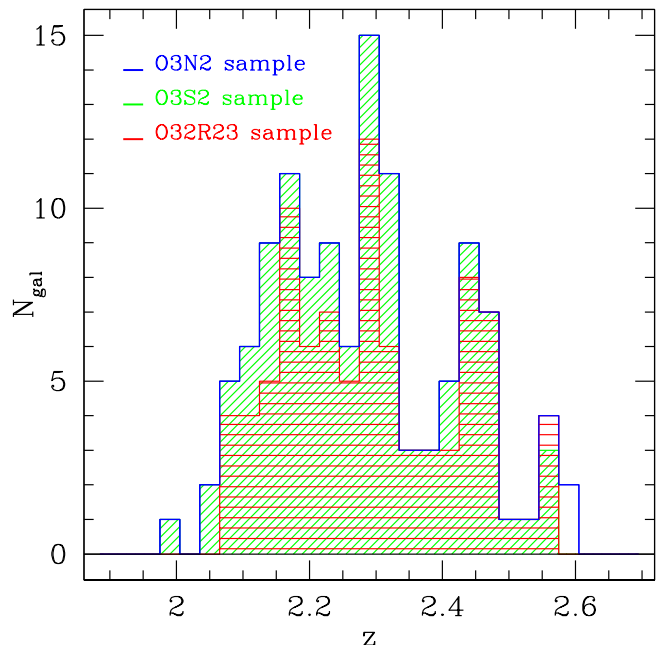


**Figure 1.** MOSFIRE redshift histograms for MOSDEF galaxies with excitation measurements. The blue histogram indicates the sample of 118 galaxies with coverage of H $\beta$ , [OIII] $\lambda 5007$ , H $\alpha$ , and [NII] $\lambda 6584$  (the [OIII] $\lambda 5007$ /H $\beta$  vs. [NII] $\lambda 6585$ /H $\alpha$  sample). The green histogram shows the sample of 115 galaxies with coverage of H $\beta$ , [OIII] $\lambda 5007$ , H $\alpha$ , and [SII] $\lambda\lambda 6717, 6731$  (the [OIII] $\lambda 5007$ /H $\beta$  vs. [SII]/H $\alpha$  sample). The red histogram denotes the sample of 89 galaxies with coverage of [OII] $\lambda\lambda 3726, 3729$ , H $\beta$ , [OIII] $\lambda 5007$ , and H $\alpha$  (the  $O_{32}$  vs.  $R_{23}$  sample). The average redshift for all three samples is  $\langle z \rangle = 2.3$ .

<sup>7</sup> In addition to data collected on observing runs specifically scheduled for the MOSDEF project, H- and K-band observations were obtained by K. Kulas, I. McLean, and G. Mace in 2013 May for one MOSDEF mask in the GOODS-N field.

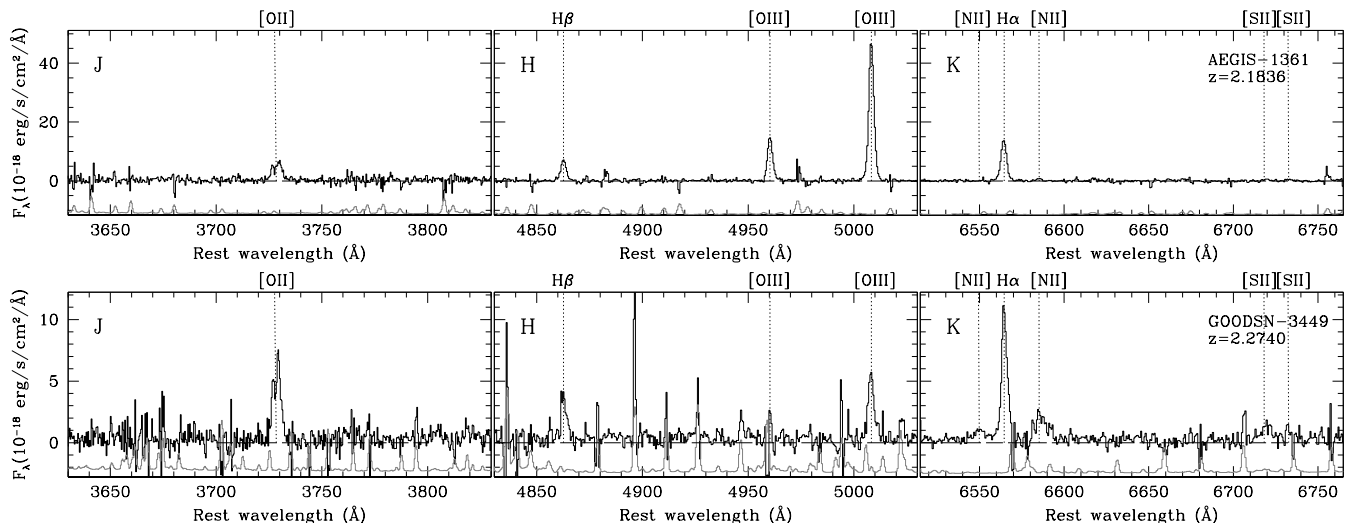


**Figure 2.** Example flux-calibrated J-band (left), H-band (center), and K-band (right) MOSFIRE spectra for two galaxies from the MOSDEF sample, demonstrating the range of observed excitation properties. The top panels show the emission-line spectrum of AEGIS-1361 ( $z = 2.1836$ ), a MOSDEF galaxy in the lowest quartile of stellar mass ( $M_* = 10^{9.53} M_\odot$ ), with lower  $[\text{NII}]\lambda 6585/\text{H}\alpha$ , and higher  $[\text{OIII}]\lambda 5007/\text{H}\beta$  and  $O_{32}$ . The bottom panels show the emission-line spectrum of GOODSN-3449 ( $z = 2.2740$ ), a MOSDEF galaxy in the highest quartile of stellar mass ( $M_* = 10^{10.67} M_\odot$ ), with higher  $[\text{NII}]\lambda 6585/\text{H}\alpha$ , and lower  $[\text{OIII}]\lambda 5007/\text{H}\beta$  and  $O_{32}$ . In each set of panels, the spectra from all filters are on the same vertical scale, which is set by the height of the strongest emission line ( $[\text{OIII}]\lambda 5007$  for AEGIS-1361 and  $\text{H}\alpha$  for GOODSN-3449). The spectra are unsmoothed and unbinned, with the wavelength scale shifted to the rest frame. The  $1\sigma$  error spectrum is plotted in grey, and offset vertically from the corresponding science spectrum in each panel.

as described in Freeman et al., in prep, we estimated galaxy sizes by counting the number of pixels above a fixed rest-frame-UV surface-brightness threshold in PSF-deconvolved *HST*/ACS images of our targets. This estimate of size should more accurately reflect the area of active star formation (either contiguous or clumpy) than the effective radius derived from a Sérsic (1968) fit to either rest-frame optical or UV profiles. We then divided dust-corrected  $\text{H}\alpha$  SFRs by rest-frame UV areas to estimate SFR surface densities ( $\Sigma_{\text{SFR}}$ ).

### 2.3. Sample

In this paper, we explore the excitation properties of  $z \sim 2.3$  star-forming galaxies, as probed by their rest-frame optical emission-line ratios. We consider the  $[\text{OIII}]\lambda 5007/\text{H}\beta$  vs.  $[\text{NII}]\lambda 6585/\text{H}\alpha$  and  $[\text{OIII}]\lambda 5007/\text{H}\beta$  vs.  $[\text{SII}]/\text{H}\alpha$  “BPT” diagrams, as well as that of  $O_{32}$  vs.  $R_{23}$ . In all plots of  $O_{32}$  and  $R_{23}$ , we have estimated the sum of  $[\text{OIII}]\lambda\lambda 4959, 5007$  fluxes as  $(1 + 1/2.98) \times [\text{OIII}]\lambda 5007$ , given that the  $[\text{OIII}]\lambda 5007/[\text{OIII}]\lambda 4959$  line ratio is fixed (Storey & Zeppen 2000) and  $[\text{OIII}]\lambda 5007$  typically offers a higher S/N measurement than  $[\text{OIII}]\lambda 4959$ .

In order to plot MOSDEF galaxies in a given emission-line diagnostic space, we require spectral coverage of all of the relevant emission lines. Furthermore, we restrict the sample to objects with no evidence for AGN activity based on either X-ray luminosity or rest-frame near-IR colors (Coil et al. 2014). To allow for systematic differences in the emission-line ratios of local and high-redshift galaxies, we do not additionally apply commonly adopted rest-frame optical AGN criteria for sample selection (e.g., Kauffmann et al. 2003; Kewley et al. 2001). Out of a parent MOSDEF sample of 133 non-AGN targets with robust MOSFIRE spectroscopic redshifts at  $1.9 \leq z \leq 2.7$ ,<sup>8</sup> 118, 115, and 89 objects, respectively,

have coverage of the lines featured in the  $[\text{OIII}]\lambda 5007/\text{H}\beta$  vs.  $[\text{NII}]\lambda 6585/\text{H}\alpha$ ,  $[\text{OIII}]\lambda 5007/\text{H}\beta$  vs.  $[\text{SII}]/\text{H}\alpha$ , and  $O_{32}$  vs.  $R_{23}$  plots.<sup>9</sup> As shown in Figure 1, the resulting redshift distributions are very similar for the three samples, with  $\langle z \rangle = 2.3$ . Furthermore, since a restriction of our analysis to the 88 galaxies with coverage in all six strong features yields qualitatively similar results, we opt to maximize the sample size for each parameter space. The galaxies in our  $z \sim 2.3$  excitation analysis span the range  $10^{9.05} - 10^{11.48} M_\odot$  in stellar mass, and  $4 - 180 M_\odot \text{ yr}^{-1}$  in dust-corrected  $\text{H}\alpha$  SFR. Figure 2 shows examples of MOSFIRE J, H, and K spectra for two galaxies drawn from the MOSDEF sample, including AEGIS-1361 ( $z = 2.1836$ ), a galaxy in the lowest-mass quartile of the sample with  $M_* = 10^{9.53} M_\odot$ , and GOODSN-3449 ( $z = 2.2740$ ), a galaxy in the highest-mass quartile with  $M_* = 10^{10.67} M_\odot$ . These spectra provide a typical representation of how the pattern of rest-frame optical emission lines varies with stellar mass.

For the study of redshift evolution in each emission-line diagnostic space, we construct  $z \sim 0$  comparison samples from the Sloan Digital Sky Survey (SDSS; York et al. 2000) Data Release 7 (DR7) catalog (Abazajian et al. 2009). Emission-line measurements (corrected for underlying stellar absorption) and galaxy properties are drawn from the MPA-JHU catalog of measurements for SDSS DR7.<sup>10</sup> Specifically, we select SDSS galaxies at

targets with only photometric redshifts prior to MOSFIRE observations turned out to be at slightly lower redshift when spectroscopically confirmed. We furthermore included serendipitous objects falling on slits and roughly within the target redshift range. We therefore use a larger redshift interval than initially designed to select galaxies for this study.

<sup>9</sup> The  $O_{32}$  vs.  $R_{23}$  sample is slightly smaller than the  $[\text{OIII}]\lambda 5007/\text{H}\beta$  vs.  $[\text{NII}]\lambda 6585/\text{H}\alpha$  and  $[\text{OIII}]\lambda 5007/\text{H}\beta$  vs.  $[\text{SII}]/\text{H}\alpha$  samples, since two of the early MOSDEF masks observed did not have J-band coverage of  $[\text{OII}]$ .

<sup>10</sup> Available at <http://www.mpa-garching.mpg.de/SDSS/DR7/>.

<sup>8</sup> Although the target redshift range is  $2.09 \leq z \leq 2.61$ , some

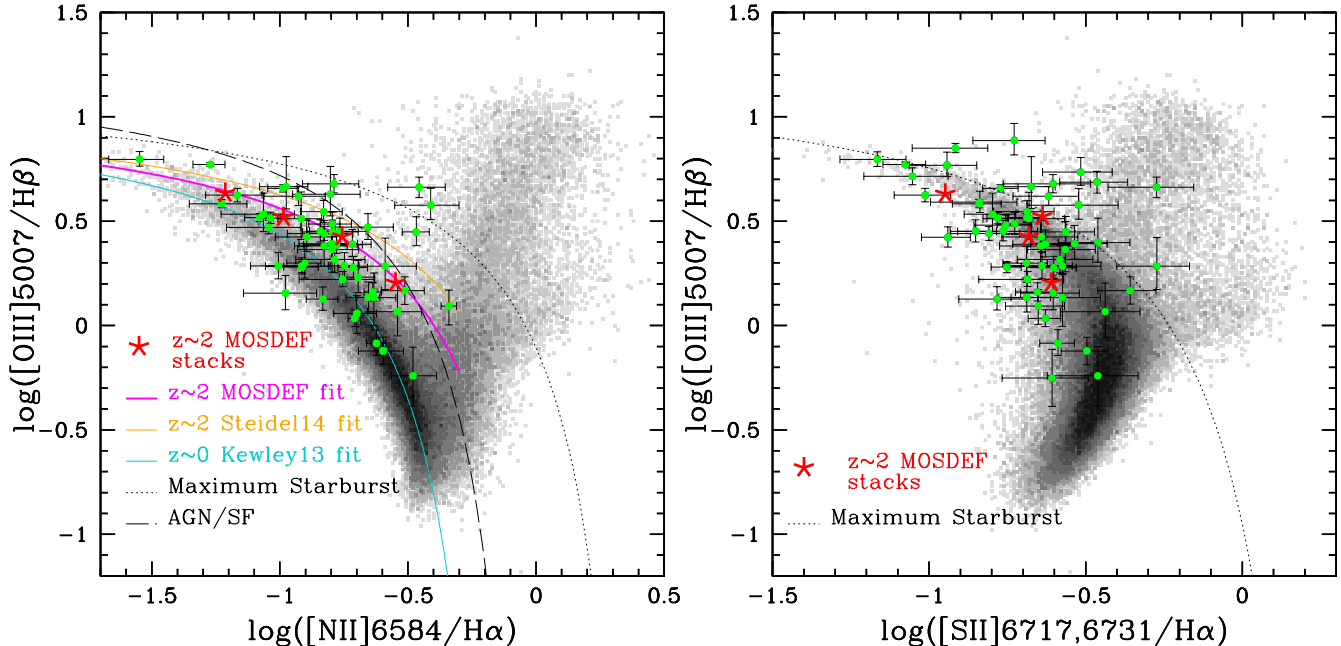


**Figure 3.** Left:  $[\text{OIII}]\lambda 5007/\text{H}\beta$  vs.  $[\text{NII}]\lambda 6585/\text{H}\alpha$  BPT diagram for  $z \sim 2.3$  MOSDEF galaxies. Green points indicate the sample of 53 MOSDEF galaxies with  $\geq 3\sigma$  detections in  $\text{H}\beta$ ,  $[\text{OIII}]\lambda 5007$ ,  $\text{H}\alpha$  and  $[\text{NII}]\lambda 6584$ . The greyscale histogram corresponds to the distribution of local SDSS galaxies. Large red stars represent measurements of stacks binned by stellar mass of all MOSDEF galaxies with coverage of the relevant emission lines regardless of whether or not lines were detected, indicating that plotting MOSDEF detections only does not result in significant bias. Stacks of increasing mass are characterized by lower  $[\text{OIII}]\lambda 5007/\text{H}\beta$  and higher  $[\text{NII}]\lambda 6584/\text{H}\alpha$ . The black dotted curve is the “maximum starburst” line from Kewley et al. (2001), while the black dashed curve is an empirical AGN/star-formation threshold from Kauffmann et al. (2003). The cyan curve indicates the  $z \sim 0$  star-forming locus (Kewley et al. 2013), while the magenta curve is the best-fit to the  $z \sim 2.3$  MOSDEF sequence. The orange curve is the best-fit to  $z \sim 2.3$  UV-selected galaxies from Steidel et al. (2014). The fit to the  $z \sim 2.3$  MOSDEF sample is not as significantly offset from the  $z \sim 0$  star-forming sequence as is the fit describing the Steidel et al. (2014) sample. Right:  $[\text{OIII}]\lambda 5007/\text{H}\beta$  vs.  $[\text{SII}]/\text{H}\alpha$  BPT diagram for  $z \sim 2.3$  MOSDEF galaxies. Symbols are as in the left-hand panel. In the  $[\text{OIII}]\lambda 5007/\text{H}\beta$  vs.  $[\text{SII}]/\text{H}\alpha$  diagram, the  $z \sim 2.3$  sample scatters symmetrically around the  $z \sim 0$  star-forming sequence.

$0.04 \leq z \leq 0.10$  to reduce aperture effects (though they are still present, even at  $z = 0.10$ ), and require  $5\sigma$  detections in the rest-frame optical emission lines featured in each diagnostic diagram. For the  $[\text{OIII}]\lambda 5007/\text{H}\beta$  vs.  $[\text{NII}]\lambda 6585/\text{H}\alpha$  and  $[\text{OIII}]\lambda 5007/\text{H}\beta$  vs.  $[\text{SII}]/\text{H}\alpha$  diagnostic diagrams, we retain all SDSS galaxies, regardless of where they fall relative to the AGN criterion of Kauffmann et al. (2003). For the  $O_{32}$  vs.  $R_{23}$  diagram, in which we focus solely on the ionization parameter and metallicity for star-forming galaxies, we reject local AGNs with the Kauffmann et al. criterion. SDSS comparison samples in  $[\text{OIII}]\lambda 5007/\text{H}\beta$  vs.  $[\text{NII}]\lambda 6585/\text{H}\alpha$  and  $[\text{OIII}]\lambda 5007/\text{H}\beta$  vs.  $[\text{SII}]/\text{H}\alpha$  spaces contain  $\sim 86,000$  galaxies, while the  $O_{32}$  vs.  $R_{23}$  comparison sample contains  $\sim 65,000$  galaxies. These comparison samples are well matched to the corresponding MOSDEF samples in terms of median stellar mass, yet they are characterized by median SFRs that are a factor of  $\sim 20$  lower.

### 3. THE EXCITATION PROPERTIES OF $Z \sim 2.3$ GALAXIES

#### 3.1. Diagnostic Diagrams

The large, rest-frame-optimally-selected sample of  $z \sim 2.3$  MOSDEF galaxies with coverage of multiple strong rest-frame optical emission lines allows for an unprecedented investigation of the excitation properties in high-redshift star-forming regions. Crucial to understanding the underlying excitation mechanisms is the consideration of multiple different diagnostic diagrams. Here

we investigate the locations of  $z \sim 2.3$  star-forming galaxies in the  $[\text{OIII}]\lambda 5007/\text{H}\beta$  vs.  $[\text{NII}]\lambda 6585/\text{H}\alpha$ ,  $[\text{OIII}]\lambda 5007/\text{H}\beta$  vs.  $[\text{SII}]/\text{H}\alpha$ , and  $O_{32}$  vs.  $R_{23}$  emission-line diagnostic diagrams.

In Figure 3, we show the MOSDEF  $z \sim 2.3$  galaxies in the space of  $[\text{OIII}]\lambda 5007/\text{H}\beta$  vs.  $[\text{NII}]\lambda 6585/\text{H}\alpha$  (left) and  $[\text{OIII}]\lambda 5007/\text{H}\beta$  vs.  $[\text{SII}]/\text{H}\alpha$  (right). We only plot galaxies with  $3\sigma$  or greater detections in the relevant emission line fluxes, leading to a sample of 53 galaxies in the  $[\text{OIII}]\lambda 5007/\text{H}\beta$  vs.  $[\text{NII}]\lambda 6585/\text{H}\alpha$  diagram and 56 in the space of  $[\text{OIII}]\lambda 5007/\text{H}\beta$  vs.  $[\text{SII}]/\text{H}\alpha$ . Given the small number (4) of objects with  $[\text{OIII}]\lambda 5007/\text{H}\beta$  upper limits in both of these samples, the requirement of  $[\text{OIII}]\lambda 5007$  detections does not result in a significant bias against galaxies with low  $[\text{OIII}]\lambda 5007/\text{H}\beta$  ratios typical of metal-rich star-forming regions. We return to the question of sample selection bias at the end of this section. For comparison, we plot SDSS galaxies in the same diagrams, along with a theoretical prediction of the  $z \sim 0$   $[\text{OIII}]\lambda 5007/\text{H}\beta$  vs.  $[\text{NII}]\lambda 6585/\text{H}\alpha$  star-forming sequence from Kewley et al. (2013), which provides a good fit to the local data.

As initially suggested by the small high-redshift samples featured in Shapley et al. (2005); Erb et al. (2006a); Liu et al. (2008), and recently confirmed by Steidel et al. (2014) using a much larger sample, the set of  $z \sim 2.3$  MOSDEF points is clearly offset on average from the  $z \sim 0$  star-forming sequence in the  $[\text{OIII}]\lambda 5007/\text{H}\beta$

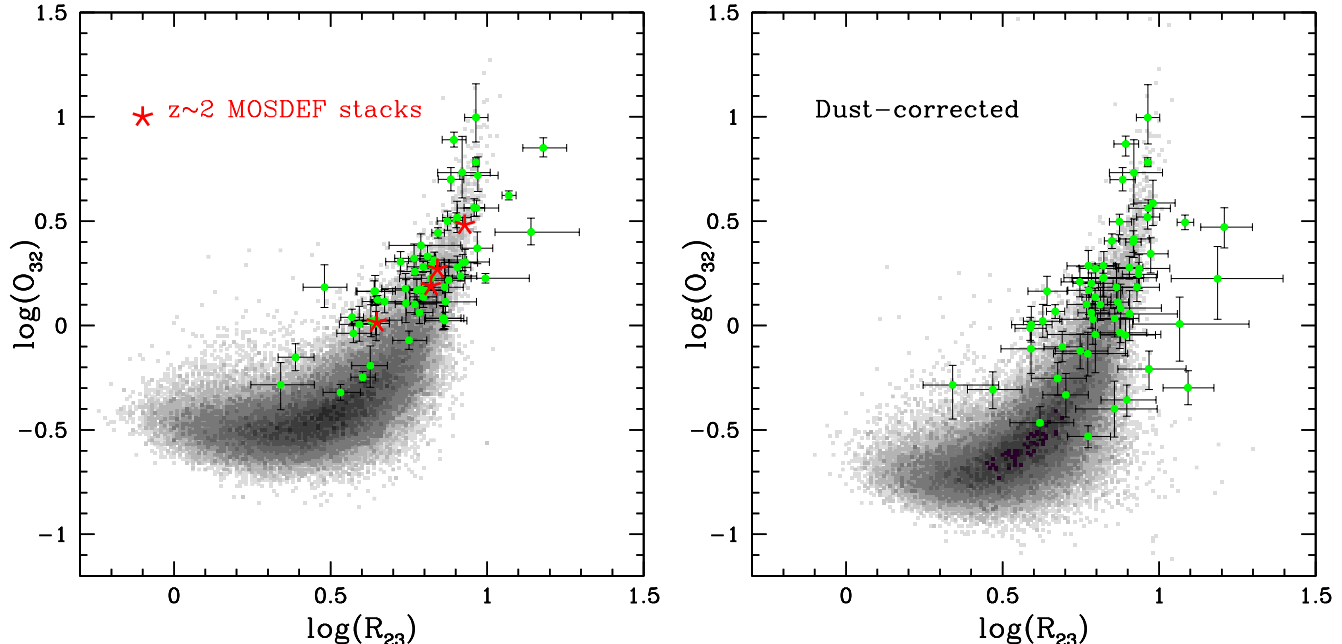


**Figure 4.** Left:  $O_{32}$  vs.  $R_{23}$  excitation diagram for  $z \sim 2.3$  MOSDEF galaxies. Symbols are as in Figure 3 for individual MOSDEF points and stacks in stellar mass, as well as SDSS galaxies. Stacks of increasing stellar mass are characterized by lower  $O_{32}$  values. The  $z \sim 2.3$  MOSDEF sample closely follows the high- $O_{32}$ , high  $R_{23}$  portion of the local excitation sequence, without evidence for a systematic offset in this parameter space. Right:  $O_{32}$  vs.  $R_{23}$  diagram, corrected for dust. Dust corrections are applied to both  $z \sim 2.3$  MOSDEF and SDSS galaxies based on the observed  $H\alpha/H\beta$  ratio (corrected for underlying stellar absorption) and assuming the Cardelli et al. (1989) attenuation curve. Dust corrections shift the observed distribution towards higher  $R_{23}$  and lower  $O_{32}$  values, but our conclusion that the  $z \sim 2.3$  MOSDEF sample follows the high-excitation portion of the local sample does not change.

vs.  $[\text{NII}]\lambda 6585/H\alpha$  diagram.<sup>11</sup> With the adoption of the same functional form as that used by Kewley et al. (2013) and Steidel et al. (2014), the best-fit to the  $z \sim 2.3$  MOSDEF sample star-forming sequence is:

$$\log([\text{OIII}]\lambda 5007/H\beta) = \frac{0.67}{\log([\text{NII}]\lambda 6585/H\alpha) - 0.20} + 1.12 \quad (1)$$

Compared with the fit to the  $z \sim 2.3$  UV-selected sample of Steidel et al. (2014) (orange curve in Figure 3), or the locus of emission-line-selected galaxies from Masters et al. (2014) at  $z \sim 1.5$  and 2.2, the sequence of rest-frame-optimally selected MOSDEF galaxies as a whole is not as offset from the local one. This difference underscores the importance of sample selection at high-redshift in determining the region occupied in the  $[\text{OIII}]\lambda 5007/H\beta$  vs.  $[\text{NII}]\lambda 6585/H\alpha$  diagram. Although the Steidel et al. (2014) sample has a similar median stellar mass to that of the  $z \sim 2.3$  MOSDEF sample ( $\sim 10^{10}M_{\odot}$ ), it spans a wider range of stellar masses (from  $10^{8.6}M_{\odot}$  to  $10^{11.4}M_{\odot}$ ) than the MOSDEF sample. Furthermore, at the lowest masses ( $< 10^{9.5}M_{\odot}$ ), galaxies in the Steidel et al. sample have higher average SFR and sSFR. The Masters et al. sample is significantly lower in mass than the MOSDEF sample, with

<sup>11</sup> We note that there are two galaxies in the MOSDEF  $[\text{OIII}]\lambda 5007/H\beta$  vs.  $[\text{NII}]\lambda 6585/H\alpha$  sample that lie above the Kewley et al. (2001) “maximum Starburst” curve in a region populated primarily by AGNs in the local universe. There is no evidence based on X-ray or rest-frame near-IR properties that these objects are AGNs (Coil et al. 2014), therefore we retain them in our sample. We note that the functional form derived for the excitation sequence of the  $z \sim 2.3$  MOSDEF sample is insensitive to the inclusion or exclusion of these two objects.

a median of  $\sim 10^9M_{\odot}$ . Given the similar range of SFRs in the Masters et al. and MOSDEF samples, the Masters et al. sample is characterized by significantly higher sSFR on average. It is crucial to understand the differences in galaxy physical properties probed by the various  $z \sim 2$  samples, and how they translate into differences in the  $[\text{OIII}]\lambda 5007/H\beta$  vs.  $[\text{NII}]\lambda 6585/H\alpha$  diagram. It is these intrinsic physical properties that modulate the integrated line ratios for a galaxy, as opposed to simply the redshift at which a galaxy is observed. Along these lines, we investigate possible causes of the difference in  $[\text{OIII}]\lambda 5007/H\beta$  vs.  $[\text{NII}]\lambda 6585/H\alpha$  star-forming sequences in section 3.2, with the separation of our sample according to various galaxy properties.

The  $[\text{OIII}]\lambda 5007/H\beta$  vs.  $[\text{SII}]/H\alpha$  BPT diagram has also been used to discriminate between star-forming galaxies and AGNs, and star-forming galaxies form a fairly well-defined sequence in this space as well. Masters et al. (2014) constructed a composite rest-frame optical spectrum from 24 emission-line galaxies at  $\langle z \rangle = 1.85$ , finding no systematic offset in the  $[\text{SII}]/H\alpha$  vs.  $[\text{OIII}]\lambda 5007/H\beta$  ratio relative to the metal-poor tail of the local star-forming sequence (see also Domínguez et al. 2013). Based on our larger sample of individual MOSDEF measurements, we confirm the lack of a systematic offset between the high-redshift galaxies and the local sequence in the  $[\text{OIII}]\lambda 5007/H\beta$  vs.  $[\text{SII}]/H\alpha$  diagram. Indeed, the high-redshift data points scatter roughly symmetrically around the star-forming SDSS points.

In addition to the two BPT diagrams, we consider the space of  $O_{32}$  vs.  $R_{23}$ , shown in Figure 4 both with (right) and without (left) nebular extinction corrections applied.

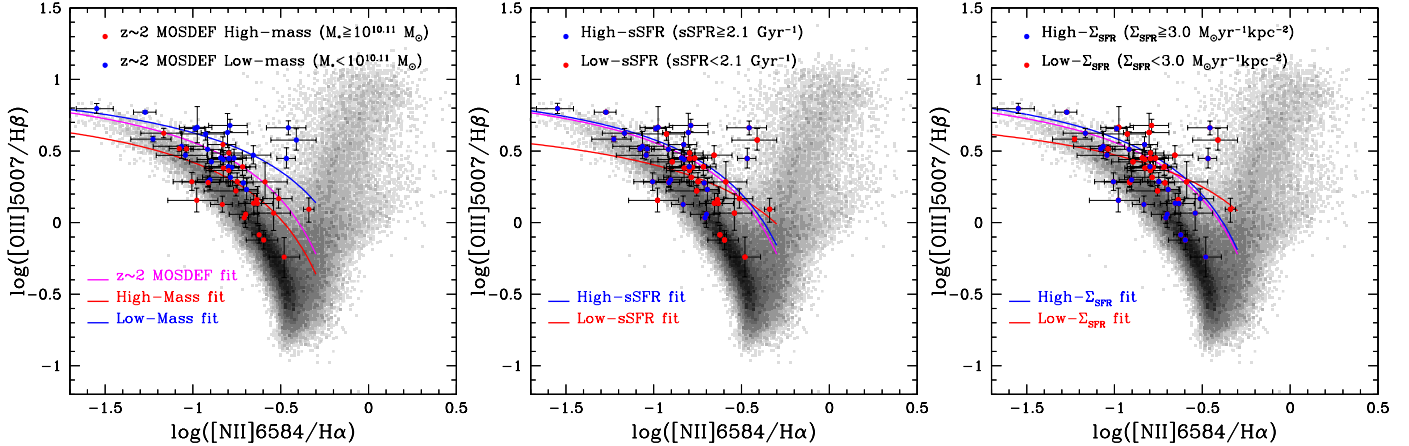


**Figure 5.**  $[\text{OIII}]\lambda 5007/\text{H}\beta$  vs.  $[\text{NII}]\lambda 6584/\text{H}\alpha$  BPT diagram, color-coded by galaxy property. In each panel blue and red points correspond to the  $z \sim 2.3$  MOSDEF sample, while the grey histogram indicates the  $z \sim 0$  SDSS sample. A fit to the full  $z \sim 2.3$  MOSDEF sample is indicated in each panel with the magenta curve, while fits to different subsamples are shown with red and blue curves. Left: Separation by stellar mass. Blue [red] symbols represent  $z \sim 2.3$  MOSDEF galaxies with stellar masses below [above] the sample median. High-mass galaxies follow the  $z \sim 0$  star-forming sequence without significant evidence for an offset, while low-mass galaxies are offset in either  $[\text{OIII}]/\text{H}\beta$  or  $[\text{NII}]/\text{H}\alpha$ . Center: Separation by sSFR. Blue [red] symbols represent  $z \sim 2.3$  MOSDEF galaxies with sSFR above [below] the sample median. The segregation by sSFR at  $z \sim 2.3$  is less clearly perpendicular to the  $z \sim 0$  star-forming sequence over the range populated by both “high” and “low” samples. Overall, the separation is more so along the sequence, with low-sSFR galaxies shifted towards higher  $[\text{NII}]/\text{H}\alpha$  values than high-sSFR galaxies. Right: Separation by  $\Sigma_{\text{SFR}}$ . Blue [red] symbols represent  $z \sim 2.3$  MOSDEF galaxies with  $\Sigma_{\text{SFR}}$  above [below] the sample median. The  $z \sim 2.3$  MOSDEF galaxies are very well-mixed as a function of  $\Sigma_{\text{SFR}}$ , with no obvious segregation.

The Cardelli et al. (1989) attenuation law was used to correct emission-line fluxes based on the observed Balmer decrement. This attenuation curve is appropriate for correcting nebular emission lines in the local universe. The attenuation law for nebular emission lines at high redshift has yet to be established, though it’s worth noting that we obtain the same key results if the attenuation curve of Calzetti et al. (2000) is used instead.  $O_{32}$  vs.  $R_{23}$  diagrams have typically been used to infer simultaneously the metallicity and ionization parameter of star-forming galaxies (e.g., Lilly et al. 2003; Nakajima et al. 2013), as both  $O_{32}$  and  $R_{23}$  are sensitive to a combination of these physical quantities. In both panels, the SDSS sample is plotted along with the  $z \sim 2.3$  MOSDEF sample. As noted by Nakajima et al. (2013) and Hainline et al. (2009), the sample of  $z \geq 2$  galaxies with  $O_{32}$  and  $R_{23}$  measurements tends to exhibit systematically higher  $O_{32}$  values than the bulk of SDSS galaxies, implying higher ionization parameters on average. The  $z \sim 2.3$  MOSDEF galaxies follow this same trend, occupying the high- $O_{32}$ , high- $R_{23}$  portion of the SDSS distribution. Yet, it is worth pointing out that there is no systematic *offset* between the high-redshift and local points. The  $z \sim 2.3$  MOSDEF sample simply occupies the low-metallicity, high-ionization-parameter tail of the local distribution. Nakajima et al. (2013) find that the sample of low-metallicity galaxies in SDSS with direct oxygen abundance estimates from Nagao et al. (2006) populate this same region of  $O_{32}$  vs.  $R_{23}$  parameter space.

In summary, although the  $z \sim 2.3$  MOSDEF sample is offset from the local star-forming sequence in the space of  $[\text{OIII}]\lambda 5007/\text{H}\beta$  vs.  $[\text{NII}]\lambda 6585/\text{H}\alpha$ , we find no evidence for a systematic offset in either of the two other diagnostic diagrams considered – i.e.,  $[\text{OIII}]\lambda 5007/\text{H}\beta$  vs.  $[\text{SII}]/\text{H}\alpha$  or  $O_{32}$  vs.  $R_{23}$ . A few notable improvements in our analysis over past work include the fact

that we feature a statistical sample of individual high-redshift  $[\text{SII}]/\text{H}\alpha$  measurements in the  $[\text{OIII}]\lambda 5007/\text{H}\beta$  vs.  $[\text{SII}]/\text{H}\alpha$  diagram, correct Balmer emission lines for underlying stellar absorption, and apply nebular extinction corrections based on the Balmer decrement to line ratios including lines that are significantly separated in wavelength (e.g.,  $O_{32}$  and  $R_{23}$ ).

One possible point of concern with our results stems from the fact that, thus far, we have used only galaxies with detections in all of the relevant emission features in order to trace out the locations of  $z \sim 2.3$  galaxies in each diagnostic diagram. This restriction leads to detections-only samples of 53, 56, and 61 galaxies, respectively, in the  $[\text{OIII}]\lambda 5007/\text{H}\beta$  vs.  $[\text{NII}]\lambda 6585/\text{H}\alpha$ ,  $[\text{OIII}]\lambda 5007/\text{H}\beta$  vs.  $[\text{SII}]/\text{H}\alpha$ , and  $O_{32}$  vs.  $R_{23}$  diagrams. For the  $[\text{OIII}]\lambda 5007/\text{H}\beta$  vs.  $[\text{NII}]\lambda 6585/\text{H}\alpha$  and  $[\text{OIII}]\lambda 5007/\text{H}\beta$  vs.  $[\text{SII}]/\text{H}\alpha$  diagrams, the detections-only samples comprise 45-50% of the MOSDEF targets with coverage of these features (largely due to the difficulty of detecting faint  $[\text{NII}]$  and  $[\text{SII}]$  lines), while this fraction is larger ( $\sim 70\%$ ) for  $O_{32}$  vs.  $R_{23}$ . In order to assess the potential bias of excluding galaxies with upper limits in line fluxes, we constructed composite spectra for the full sample in each emission-line space in four bins of increasing stellar mass, with roughly equal numbers of galaxies in each bin. With stellar mass estimates for all MOSDEF galaxies, this property provides a natural basis for dividing the sample. For the  $[\text{OIII}]\lambda 5007/\text{H}\beta$  vs.  $[\text{NII}]\lambda 6585/\text{H}\alpha$  and  $[\text{OIII}]\lambda 5007/\text{H}\beta$  vs.  $[\text{SII}]/\text{H}\alpha$  samples, we made composite K and H-band spectra, covering, respectively  $\text{H}\alpha + [\text{NII}]\lambda 6584 + [\text{SII}]\lambda, \lambda 6717, 6731$ , and  $[\text{OIII}]\lambda 5007 + \text{H}\beta$ , while, for  $O_{32}$  vs.  $R_{23}$ , we made stacks in H and J, covering, respectively,  $[\text{OIII}]\lambda 5007 + \text{H}\beta$  and  $[\text{OII}]\lambda 3727$ . Individual spectra in each filter were shifted to the rest frame, converted from flux- to luminosity-density units (i.e.,  $\text{erg s}^{-1} \text{\AA}^{-1}$ ), and normalized by  $\text{H}\alpha$  luminosity in order to obtain the av-

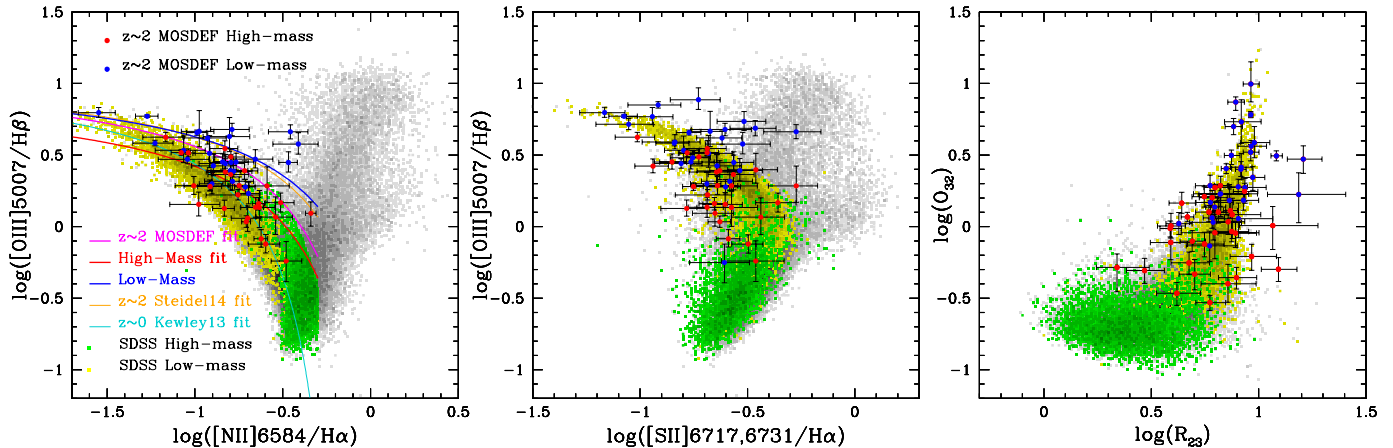


**Figure 6.**  $[\text{OIII}]\lambda 5007/\text{H}\beta$  vs.  $[\text{NII}]\lambda 6585/\text{H}\alpha$ ,  $[\text{OIII}]\lambda 5007/\text{H}\beta$  vs.  $[\text{SII}]\lambda 6717, 6731/\text{H}\alpha$ , and  $O_{32}$  vs.  $R_{23}$  diagrams, segregated by stellar mass. In each panel,  $z \sim 2.3$  MOSDEF galaxies are indicated with blue (low-mass) and red (high-mass) points. The median (dividing) mass is  $10^{10.1} M_{\odot}$  for the  $[\text{OIII}]\lambda 5007/\text{H}\beta$  vs.  $[\text{NII}]\lambda 6585/\text{H}\alpha$  and  $[\text{OIII}]\lambda 5007/\text{H}\beta$  vs.  $[\text{SII}]\lambda 6717, 6731/\text{H}\alpha$  samples, and  $10^{9.9} M_{\odot}$  for the  $O_{32}$  vs.  $R_{23}$  sample, with the difference for  $O_{32}$  vs.  $R_{23}$  resulting from the slightly different sample demographics for this diagram (see Section 2.3). SDSS star-forming galaxies (i.e., those that fall below the curve of Kauffmann et al. 2003) are shown with small yellow (low-mass, i.e.,  $M_{*} < 10^{9.25} M_{\odot}$ ) and green (high-mass, i.e.,  $M_{*} > 10^{10.52} M_{\odot}$ ) points. In each excitation diagram, low- and high-mass SDSS galaxies separate along the excitation sequence. Left:  $[\text{OIII}]\lambda 5007/\text{H}\beta$  vs.  $[\text{NII}]\lambda 6585/\text{H}\alpha$  diagram. The  $z \sim 0$  star-forming sequence, as well as the fits to the overall  $z \sim 2.3$  MOSDEF and Steidel et al. (2014) samples are indicated as in Figure 3. Additionally, we show fits to the low-mass and high-mass  $z \sim 2.3$  subsamples using, respectively, blue and red curves. The fit to the low-mass portion of the  $z \sim 2.3$  MOSDEF sample is indistinguishable from the Steidel et al. (2014) sequence, while the fit to the high-mass  $z \sim 2.3$  MOSDEF galaxies is very similar to the  $z \sim 0$  star-forming sequence. Center:  $[\text{OIII}]\lambda 5007/\text{H}\beta$  vs.  $[\text{SII}]\lambda 6717, 6731/\text{H}\alpha$  diagram. Low-mass  $z \sim 2.3$  MOSDEF galaxies are offset towards higher  $[\text{OIII}]/\text{H}\beta$  ratios, but both the low- and high-mass portions of the MOSDEF sample overlap significantly with the  $z \sim 0$  star-forming sequence. Right: Dust-corrected  $O_{32}$  vs.  $R_{23}$  diagram. The low- and high-mass  $z \sim 2.3$  MOSDEF subsamples separate cleanly along the  $O_{32}$  vs.  $R_{23}$  excitation sequence, just as the SDSS galaxies do.

erage line ratios in each bin in stellar mass. Requiring the detection of  $\text{H}\alpha$  to normalize the individual spectra slightly reduces the  $[\text{OIII}]\lambda 5007/\text{H}\beta$  vs.  $[\text{NII}]\lambda 6585/\text{H}\alpha$ ,  $[\text{OIII}]\lambda 5007/\text{H}\beta$  vs.  $[\text{SII}]\lambda 6717, 6731/\text{H}\alpha$ , and  $O_{32}$  vs.  $R_{23}$  sample sizes to 106, 105, and 84 galaxies, respectively, ( $\geq 90\%$  of the full samples with coverage of the relevant emission lines) but should not result in a significant bias. Stacked spectra for each stellar-mass bin (in each filter) were then constructed as straight averages of the individual rest-frame,  $\text{H}\alpha$ -normalized spectra. Emission-line ratios in each composite spectrum were measured by fitting Gaussian profiles to the  $\text{H}\alpha$ ,  $[\text{NII}]$ ,  $[\text{OIII}]$ , and  $\text{H}\beta$  features, and performing simple integration over  $[\text{OII}]$  and  $[\text{SII}]$ . Composite line ratios including  $\text{H}\alpha$  and  $\text{H}\beta$  were corrected for underlying Balmer absorption using the median Balmer absorption correction among individually-detected galaxies in each bin. For  $O_{32}$  vs.  $R_{23}$ , we construct the stacks without correction for dust extinction given that we do not have individual  $\text{H}\alpha$  and  $\text{H}\beta$  detections for all objects being combined. However, these stacks should still indicate how representative the observed  $O_{32}$  and  $R_{23}$  ratios are for individual detections-only objects. As shown in Figures 3 and 4, the stacked data points fall well within the distribution of individual detections, thus suggesting that we are not introducing significant bias by considering detections only.

### 3.2. Excitation vs. Galaxy Properties

In the local universe, Brinchmann et al. (2008) found that, at fixed stellar mass, galaxies with higher  $\text{H}\alpha$  EWs (a proxy for sSFR) are offset towards higher  $[\text{NII}]/\text{H}\alpha$  and  $[\text{OIII}]/\text{H}\beta$  in the  $[\text{OIII}]\lambda 5007/\text{H}\beta$  vs.  $[\text{NII}]\lambda 6585/\text{H}\alpha$  BPT diagram. Liu et al. (2008) found that SDSS galaxies with higher concentrations and  $\Sigma_{\text{SFR}}$  values (again at fixed stellar mass) tended to be offset in the same

sense as high-redshift galaxies in the  $[\text{OIII}]\lambda 5007/\text{H}\beta$  vs.  $[\text{NII}]\lambda 6585/\text{H}\alpha$  BPT diagram. To delve into the cause of anomalous properties of  $z \sim 2.3$  star-forming galaxies relative to local samples in the space of  $[\text{OIII}]\lambda 5007/\text{H}\beta$  vs.  $[\text{NII}]\lambda 6585/\text{H}\alpha$ , we investigate the dependence of location in the  $[\text{OIII}]\lambda 5007/\text{H}\beta$  vs.  $[\text{NII}]\lambda 6585/\text{H}\alpha$  diagram as a function of multiple different galaxy properties. We separate the  $[\text{OIII}]\lambda 5007/\text{H}\beta$  vs.  $[\text{NII}]\lambda 6585/\text{H}\alpha$  MOSDEF sample into “high” and “low” bins according to  $M_{*}$ , sSFR, and  $\Sigma_{\text{SFR}}$ , using the sample median of each property ( $M_{*,\text{med}} = 10^{10.11} M_{\odot}$ ,  $\text{sSFR}_{\text{med}} = 2.4 \text{ Gyr}^{-1}$ , and  $\Sigma_{\text{SFR},\text{med}} = 3.2 M_{\odot} \text{ yr}^{-1} \text{ kpc}^{-2}$ ) to demarcate the bins. In Figure 5, we color-code  $z \sim 2.3$  MOSDEF galaxies in the  $[\text{OIII}]\lambda 5007/\text{H}\beta$  vs.  $[\text{NII}]\lambda 6585/\text{H}\alpha$  diagram by property, with high-mass [low-sSFR, low- $\Sigma_{\text{SFR}}$ ] points indicated in red, and low-mass [high-sSFR, high- $\Sigma_{\text{SFR}}$ ] points in blue. Separate fits to the “high”- and “low”-mass  $[\text{sSFR}, \Sigma_{\text{SFR}}]$  star-forming sequences are also indicated in each panel.

The most striking segregation perpendicular to the local excitation sequence is with stellar mass. The low-mass MOSDEF galaxies occupy a region of  $[\text{OIII}]\lambda 5007/\text{H}\beta$  vs.  $[\text{NII}]\lambda 6585/\text{H}\alpha$  parameter space almost completely disjoint from that of the SDSS sample. Furthermore, as shown in Figure 6 (left), a fit to the star-forming sequence of the low-mass MOSDEF galaxies is basically indistinguishable from the one derived by Steidel et al. (2014) for UV-selected galaxies. At the same time, the high-mass half of the MOSDEF sample shows no significant offset relative to the SDSS sequence. Neither sSFR nor  $\Sigma_{\text{SFR}}$  shows the same degree of separation perpendicular to the SDSS star-forming sequence, in contrast to what is observed in the local universe. With sSFR, galaxies separate primarily along the dimension

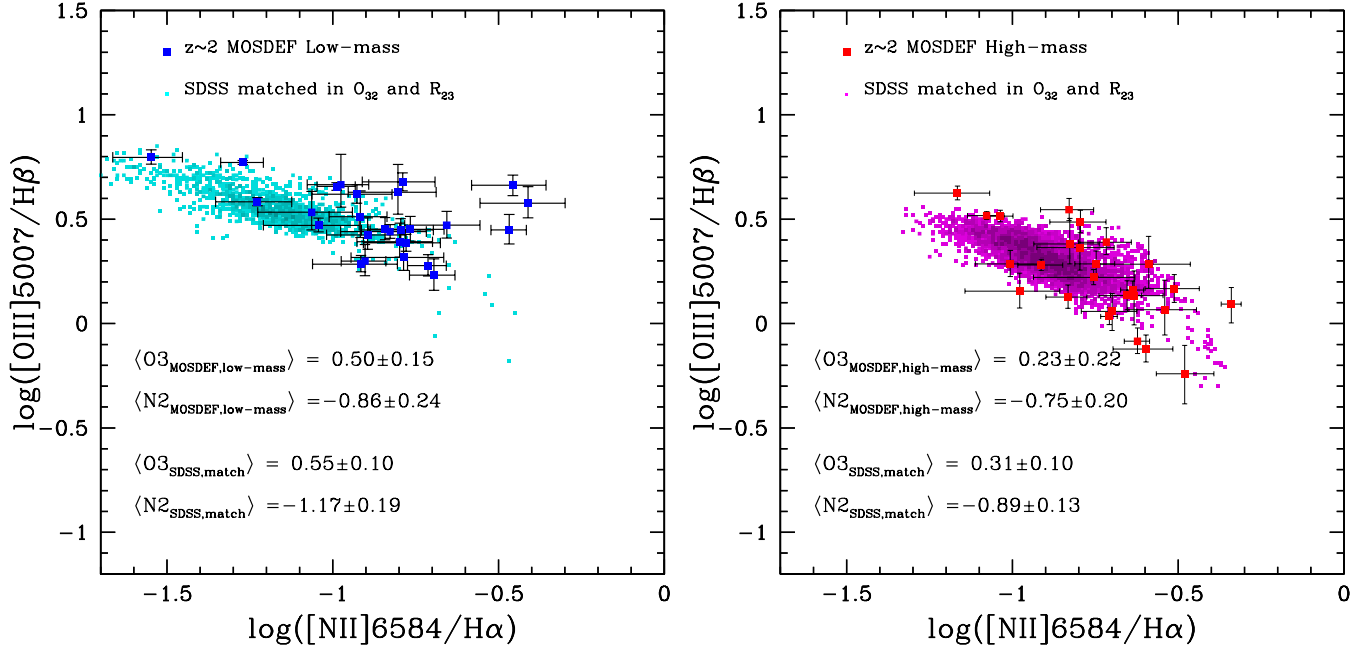


**Figure 7.**  $[\text{OIII}]\lambda 5007/\text{H}\beta$  vs.  $[\text{NII}]\lambda 6585/\text{H}\alpha$  BPT diagrams for low- and high-mass  $z \sim 2.3$  MOSDEF galaxies, along with matched SDSS samples. In each panel, the SDSS sample (small points) has been selected to match the  $z \sim 2.3$  MOSDEF subsample in average  $\log(O_{32})$  and  $\log(R_{23})$ , and the sample mean and standard deviation for O3 and N2 are listed for both MOSDEF and SDSS samples. Given the MOSDEF and SDSS comparison sample sizes, the error on the mean is a factor of  $\sim 5$  smaller than the sample standard deviation for all MOSDEF samples, and negligible for the SDSS comparison samples. Left: Low-mass MOSDEF galaxies (blue points) and SDSS galaxies with matching  $O_{32}$  and  $R_{23}$  (small cyan points) have very similar mean O3 ( $\log([\text{OIII}]\lambda 5007/\text{H}\beta)$ ), while N2 ( $\log([\text{NII}]\lambda 6585/\text{H}\alpha)$ ) is offset towards higher values for the  $z \sim 2.3$  MOSDEF galaxies. Right: High-mass MOSDEF galaxies (red points) and SDSS galaxies with matching  $O_{32}$  and  $R_{23}$  (small purple points) have very similar values for both mean O3 and N2.

of  $[\text{NII}]/\text{H}\alpha$ , and, with  $\Sigma_{\text{SFR}}$ , galaxies from the “high” and “low” samples are well-mixed in both dimensions. Due to the limited sample size of the early MOSDEF dataset, we are not able to perform the same experiment that Brinchmann et al. (2008) and Liu et al. (2008) did, looking for separation in  $\text{sSFR}$  and  $\Sigma_{\text{SFR}}$  at fixed stellar mass. Such analyses will be possible with the full MOSDEF dataset.

Given the clear separation according to stellar mass in the  $[\text{OIII}]\lambda 5007/\text{H}\beta$  vs.  $[\text{NII}]\lambda 6585/\text{H}\alpha$  diagram, we also investigate how high- and low-mass MOSDEF galaxies populate the  $[\text{OIII}]\lambda 5007/\text{H}\beta$  vs.  $[\text{SII}]/\text{H}\alpha$  and  $O_{32}$  vs.  $R_{23}$  diagrams (Figure 6). In all three panels, we color-code star-forming SDSS points by stellar mass. To accentuate the fact that the mean stellar mass varies smoothly along the local star-forming sequences in  $[\text{OIII}]\lambda 5007/\text{H}\beta$  vs.  $[\text{NII}]\lambda 6585/\text{H}\alpha$ ,  $[\text{OIII}]\lambda 5007/\text{H}\beta$  vs.  $[\text{SII}]/\text{H}\alpha$ , and  $O_{32}$  vs.  $R_{23}$ , we only plot the low-mass ( $M_* < 10^{9.25} M_\odot$ ; yellow) and high-mass ( $M_* > 10^{10.52} M_\odot$ ; green) tails of the SDSS stellar mass distribution.

In the  $[\text{OIII}]\lambda 5007/\text{H}\beta$  vs.  $[\text{SII}]/\text{H}\alpha$  diagram, although low-mass galaxies have larger  $[\text{OIII}]/\text{H}\beta$  ratios on average than high-mass galaxies (by  $\sim 0.3$  dex), both low- and high-mass samples show significant overlap with the  $z \sim 0$  star-forming sequence. Furthermore, given the shape of the  $z \sim 0$   $[\text{OIII}]\lambda 5007/\text{H}\beta$  vs.  $[\text{SII}]/\text{H}\alpha$  star-forming sequence (i.e., more “vertical” than the  $[\text{OIII}]\lambda 5007/\text{H}\beta$  vs.  $[\text{NII}]\lambda 6585/\text{H}\alpha$  sequence), the separation by mass at  $z \sim 2.3$  is not obviously inconsistent with the manner in which local galaxies separate by mass (i.e., low-mass galaxies primarily show higher  $[\text{OIII}]/\text{H}\beta$ , although the low- and high-mass samples significantly

overlap in  $[\text{SII}]/\text{H}\alpha$  as the star-forming sequence curves back on itself). In contrast, the separation of low- and high-mass MOSDEF galaxies in the  $[\text{OIII}]\lambda 5007/\text{H}\beta$  vs.  $[\text{NII}]\lambda 6585/\text{H}\alpha$  diagram extends in a direction almost perpendicular to the sense in which low- and high-mass galaxies segregate along the local  $[\text{OIII}]\lambda 5007/\text{H}\beta$  vs.  $[\text{NII}]\lambda 6585/\text{H}\alpha$  sequence.

In the  $O_{32}$  vs.  $R_{23}$  panel, the separation of low- and high-mass MOSDEF galaxies is entirely parallel to the local star-forming sequence and the sense in which local galaxies segregate, with low-mass objects showing both significantly higher  $O_{32}$  values and slightly higher values of  $R_{23}$ . One final point is that, in all panels, the MOSDEF sample is entirely contained within the region dominated by low-mass ( $M_* < 10^{9.25} M_\odot$ ) SDSS galaxies – i.e., the  $z \sim 2.3$  sample shows excitation properties characteristic of low-mass galaxies in the local universe. We return to this point in section 4.

### 3.3. An offset in N2 or O3?

In order to understand the underlying cause of the offset in the  $[\text{OIII}]\lambda 5007/\text{H}\beta$  vs.  $[\text{NII}]\lambda 6585/\text{H}\alpha$  BPT diagram, it is important to determine the manner in which the high-redshift systems are actually different from local galaxies. Specifically, we would like to distinguish among the possibilities that galaxies with a given set of physical properties (e.g., metallicity) have higher  $[\text{OIII}]/\text{H}\beta$  ratios (O3), higher  $[\text{NII}]/\text{H}\alpha$  ratios (N2), or both higher O3 and N2 values. MOSDEF measurements in multiple diagnostic diagrams enable this investigation. Figures 3 and 4 already suggest that emission diagnostics involving nitrogen are the source of the anomaly. With the use

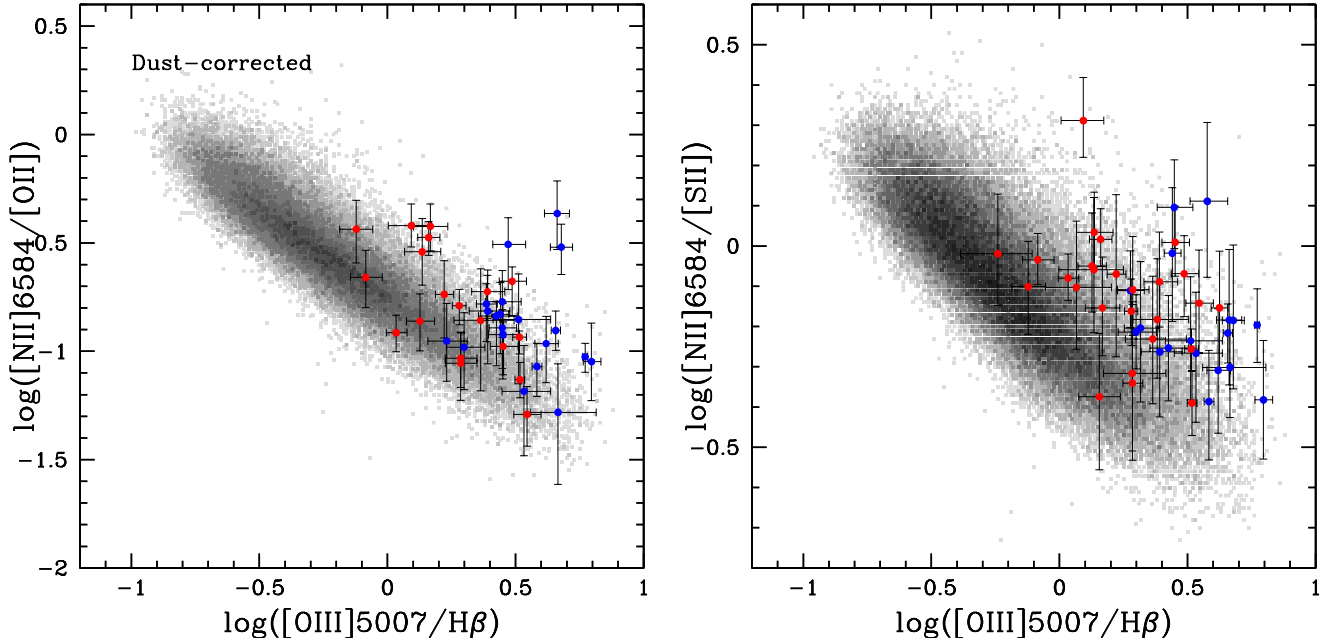


**Figure 8.** Left: N2O2 vs.  $[\text{OIII}]/\text{H}\beta$ . Symbols are as in Figure 5, with low- and high-mass  $z \sim 2.3$  MOSDEF galaxies indicated, respectively, with blue and red points. N2O2 values have been corrected for dust extinction, given the wide wavelength baseline between  $[\text{NII}]\lambda 6584$  and  $[\text{OII}]\lambda\lambda 3726, 3729$ . Among the low-mass  $z \sim 2.3$  MOSDEF galaxies (those at the highest  $[\text{OIII}]/\text{H}\beta$  values), there is an offset towards higher N2O2 at fixed  $[\text{OIII}]/\text{H}\beta$ , which we interpret as an elevated N/O abundance ratio at fixed oxygen abundance. At higher masses in the  $z \sim 2.3$  sample, there is less evidence for an elevated N/O ratio. Right: N2S2 vs.  $[\text{OIII}]/\text{H}\beta$ . Again, symbols are as in Figure 5. Independent of stellar mass,  $z \sim 2.3$  MOSDEF galaxies are offset towards higher N2S2 values at fixed  $[\text{OIII}]/\text{H}\beta$ . This trend may indicate evidence for variations in S/O ratios when considered together with the N2O2 vs.  $[\text{OIII}]/\text{H}\beta$  diagram.

of the  $O_{32}$  vs.  $R_{23}$  diagram, we can provide a definitive demonstration that this is the case. In the  $O_{32}$  vs.  $R_{23}$  diagram,  $z \sim 2.3$  MOSDEF galaxies closely follow the distribution of the local SDSS sample, albeit occupying the high- $O_{32}$ , high- $R_{23}$  portion of the local excitation sequence. Accordingly, it is possible to construct a sample of SDSS galaxies that matches a given set of MOSDEF galaxies in mean  $O_{32}$  and  $R_{23}$ , and then compare the distributions of O3 and N2 for both the MOSDEF and matched SDSS samples. We construct matched SDSS samples for both low-mass ( $M_* < 10^{10.11} M_\odot$ ) and high-mass ( $M_* \geq 10^{10.11} M_\odot$ ) MOSDEF galaxies and plot the matched MOSDEF and SDSS samples in the space of  $[\text{OIII}]\lambda 5007/\text{H}\beta$  vs.  $[\text{NII}]\lambda 6585/\text{H}\alpha$  (Figure 7), along with an indication of the sample mean O3 and N2 values. The high-mass MOSDEF and matched SDSS samples follow very similar distributions in  $[\text{OIII}]\lambda 5007/\text{H}\beta$  vs.  $[\text{NII}]\lambda 6585/\text{H}\alpha$ , with similar mean O3 and N2 values within the errors. Although the low-mass MOSDEF and matched SDSS sample have very similar mean O3 values, the low-mass MOSDEF sample is offset towards higher N2 values. This analysis demonstrates that the offset in the  $z \sim 2.3$   $[\text{OIII}]\lambda 5007/\text{H}\beta$  vs.  $[\text{NII}]\lambda 6585/\text{H}\alpha$  BPT diagram should be understood in terms of low-mass  $z \sim 2$  MOSDEF galaxies having higher  $[\text{NII}]/\text{H}\alpha$  ratios on average, at fixed  $[\text{OIII}]/\text{H}\beta$ . Alternatively, we can state that, at fixed  $O_{32}$  and  $R_{23}$ , which, as we argue in section 4.2, serves as a proxy for oxygen abundance, low-mass  $z \sim 2.3$  MOSDEF galaxies have higher  $[\text{NII}]/\text{H}\alpha$  ratios than their  $z \sim 0$  counterparts.

#### 4. DISCUSSION

##### 4.1. The $[\text{NII}]/\text{H}\alpha$ Offset in the $[\text{OIII}]\lambda 5007/\text{H}\beta$ vs. $[\text{NII}]\lambda 6585/\text{H}\alpha$ BPT Diagram

There are several different effects that have been considered to explain the observed offset in the  $[\text{OIII}]\lambda 5007/\text{H}\beta$  vs.  $[\text{NII}]\lambda 6585/\text{H}\alpha$  BPT diagram among high-redshift galaxies. First, there are the physical parameters describing the H II regions contributing to the integrated line ratios from galaxies. These include the ionization parameter, ionizing spectrum of the stars illuminating the H II-region gas, and the electron density. Early work highlighting the issue of the high-redshift offset in the  $[\text{OIII}]\lambda 5007/\text{H}\beta$  vs.  $[\text{NII}]\lambda 6585/\text{H}\alpha$  BPT diagram focused on these parameters (e.g., Shapley et al. 2005; Liu et al. 2008; Brinchmann et al. 2008), and they have been revisited more recently by Kewley et al. (2013), Steidel et al. (2014), and Masters et al. (2014). Systematically higher ionization parameters (which appear to apply in high-redshift galaxies; Nakajima et al. 2013), harder ionizing spectra, and higher electron densities (Shirazi et al. 2014), all tend to shift the locus of galaxies in the  $[\text{OIII}]\lambda 5007/\text{H}\beta$  vs.  $[\text{NII}]\lambda 6585/\text{H}\alpha$  diagram towards higher  $[\text{OIII}]/\text{H}\beta$  and  $[\text{NII}]/\text{H}\alpha$  values. Next, there is the role of different types of pressure in determining the internal structure and dynamics of H II regions. Yeh et al. (2013) and Verdolini et al. (2013) suggest that radiation pressure is significant in high-redshift H II regions, as compared with gas pressure associated with stellar winds, and that the effects of radiation pressure can lead to  $[\text{OIII}]/\text{H}\beta$  line ratios in excess of the “maximum starburst” limit of Kewley et al. (2001). Possible contamination by weak AGNs has also been suggested as a way to shift galaxy emission-line ratios into the “composite” region of the  $[\text{OIII}]\lambda 5007/\text{H}\beta$

vs. [NII] $\lambda 6585$ /H $\alpha$  BPT diagram (e.g., Wright et al. 2010), in between the curves of Kauffmann et al. (2003) and Kewley et al. (2001). Finally, both Masters et al. (2014) and Steidel et al. (2014) consider gas-phase abundance ratios – specifically, the N/O ratio – which can affect where galaxies fall in the [OIII] $\lambda 5007$ /H $\beta$  vs. [NII] $\lambda 6585$ /H $\alpha$  BPT diagram. If the relationship between N/O and  $12 + \log(\text{O}/\text{H})$  evolves out to high redshift, then distant galaxies will shift relative to local ones in the [OIII] $\lambda 5007$ /H $\beta$  vs. [NII] $\lambda 6585$ /H $\alpha$  BPT diagram.

In order to distinguish among these different scenarios, it is crucial to consider the full set of strong rest-frame optical emission lines. These include not only H $\beta$ , [OIII] $\lambda 5007$ , H $\alpha$ , and [NII] $\lambda 6584$ , which comprise the [OIII] $\lambda 5007$ /H $\beta$  vs. [NII] $\lambda 6585$ /H $\alpha$  BPT measurements, but also [OII] $\lambda \lambda 3726, 3729$  and [SII] $\lambda, \lambda 6717, 6731$ . With the  $z \sim 2.3$  MOSDEF dataset, we are in the unique position of covering this full set of lines for a statistical sample of galaxies. Accordingly, we investigate both [OIII] $\lambda 5007$ /H $\beta$  vs. [NII] $\lambda 6585$ /H $\alpha$  and [OIII] $\lambda 5007$ /H $\beta$  vs. [SII]/H $\alpha$  BPT diagrams, as well as the space of  $O_{32}$  vs.  $R_{23}$ . Based on a single composite spectrum of 26 emission-line selected galaxies at  $1.3 \leq z \leq 2.3$ , Masters et al. (2014) found that the observed offset in the [OIII] $\lambda 5007$ /H $\beta$  vs. [NII] $\lambda 6585$ /H $\alpha$  BPT diagram did not appear in the space of [OIII] $\lambda 5007$ /H $\beta$  vs. [SII]/H $\alpha$ . We confirm this same trend, using a larger sample of individual measurements. Specifically, the MOSDEF sample scatters symmetrically around the  $z \sim 0$  star-forming sequence in the [OIII] $\lambda 5007$ /H $\beta$  vs. [SII]/H $\alpha$  BPT diagram, and does not suggest a systematic offset. Even more striking is the distribution of MOSDEF galaxies in the  $O_{32}$  vs.  $R_{23}$  diagram, which is completely based on oxygen and hydrogen emission lines. In this space, the  $z \sim 2.3$  MOSDEF sample scatters along the local sequence, with no evidence for an offset perpendicular to the locus of  $z \sim 0$  galaxies. Although the  $z \sim 2.3$  galaxies only occupy the high- $O_{32}$ , high- $R_{23}$  tail of the local distribution, we can identify direct analogs for high-redshift galaxies in the space of  $O_{32}$  vs.  $R_{23}$ . We use this match to uncover the nature of the [OIII] $\lambda 5007$ /H $\beta$  vs. [NII] $\lambda 6585$ /H $\alpha$  offset among low-mass  $z \sim 2.3$  MOSDEF galaxies, finding that SDSS galaxies matched to  $z \sim 2.3$  samples in average  $O_{32}$  and  $R_{23}$  are also roughly matched in average [OIII]/H $\beta$ . The offset for these low-mass  $z \sim 2.3$  MOSDEF galaxies is found in their [NII]/H $\alpha$  ratios. Indeed, at fixed  $O_{32}$ ,  $R_{23}$ , and [OIII]/H $\beta$ , the  $z \sim 2.3$  galaxies offset in the [OIII] $\lambda 5007$ /H $\beta$  vs. [NII] $\lambda 6585$ /H $\alpha$  BPT diagram show higher average [NII]/H $\alpha$  ratios than their SDSS counterparts.

As in Masters et al. (2014), we interpret this offset as a difference in N/O abundance ratio at fixed metallicity. We find further evidence of a deviation in N/O when considering the [NII] $\lambda 6584$ /[OII] $\lambda \lambda 3726, 3729$  ratio (N2O2). N2O2 has been calibrated by Pérez-Montero & Contini (2009) for local galaxies as a proxy for the N/O abundance ratio ( $\log(\text{N}/\text{O}) = 0.93 \times \text{N2O2} - 0.20$ ). In order to compare with SDSS, we plot N2O2 as a function of [OIII] $\lambda 5007$ /H $\beta$ . Since the set of excitation diagrams we have considered here collectively suggest that [NII]/H $\alpha$  is the anomalous line ratio at high redshift, [OIII] $\lambda 5007$ /H $\beta$  serves as a better control variable than [NII]/H $\alpha$ , and is anti-correlated with oxygen abundance in the regime

that we consider here (Maiolino et al. 2008). For the low-mass portion of the MOSDEF sample, corresponding to the highest [OIII]/H $\beta$  ratios ( $\langle \log([\text{OIII}]/\text{H}\beta) \rangle = 0.5$ ), Figure 8 (left) demonstrates that MOSDEF galaxies are characterized by higher N2O2 ratios on average relative to SDSS galaxies with similar [OIII]/H $\beta$  ratios. This average offset corresponds to  $\Delta \text{N2O2} = 0.24$  dex. For the high-mass portion of the MOSDEF sample (at lower [OIII]/H $\beta$  ratios), there is better agreement between  $z \sim 2.3$  MOSDEF and SDSS galaxies. This result provides additional support for higher N/O ratios at fixed oxygen abundance among  $z \sim 2.3$  MOSDEF galaxies with  $M \leq 10^{10.11} M_{\odot}$ .

Pérez-Montero & Contini (2009) also provide a calibration between [NII] $\lambda 6584$ /[SII] $\lambda \lambda 6717, 6731$  ratio (N2S2) and N/O ( $\log(\text{N}/\text{O}) = 1.26 \times \text{N2S2} - 0.86$ ). This relationship is characterized by more scatter than the one using N2O2, possibly due to variations in the S/O abundance ratio in galaxies. We show the relation between N2S2 and [OIII]/H $\beta$  for  $z \sim 2.3$  MOSDEF and SDSS galaxies in Figure 8 (right), uncovering an offset towards higher N2S2 at fixed [OIII]/H $\beta$ , independent of [OIII]/H $\beta$  (i.e., mass). Exactly why the behavior of N2S2 and N2O2 differ in detail at high mass is beyond the scope of the current work, as is detailed photoionization modeling to constrain the nature of high-redshift ionizing spectra and ionization parameters, and the significance of radiation pressure in determining H II region structure and dynamics. However, with our unique, multi-dimensional dataset, we establish that, at low-mass,  $z \sim 2.3$  MOSDEF galaxies consistently show an offset towards higher N/O ratios at fixed [OIII]/H $\beta$ , relative to the SDSS sample. In order to investigate potential differences in ionizing spectra and ionization parameters at high redshift, photoionization models tuned to match the locus of high-redshift galaxies in the [OIII] $\lambda 5007$ /H $\beta$  vs. [NII] $\lambda 6585$ /H $\alpha$  diagram alone (e.g., Steidel et al. 2014) must now be compared with observations of the [OIII] $\lambda 5007$ /H $\beta$  vs. [SII]/H $\alpha$  and  $O_{32}$  vs.  $R_{23}$  diagrams. Such comparisons are required to test the general validity of these models.

Masters et al. (2014) and Steidel et al. (2014) offer differing explanations for elevated N/O ratios in high-redshift, actively star-forming galaxies. Masters et al. (2014) attribute this abundance signature to enhanced populations of Wolf-Rayet stars in  $z \sim 2$  stellar populations, whose nitrogen-rich winds (from WN-sequence Wolf-Rayet stars) mix with the ISM to enrich future generations of stars. Such a scenario relies on catching galaxies at extremely young stellar population ages, when the signatures of Wolf-Rayet stars are most prominent in integrated spectra (Shapley et al. 2003). This timing requirement may prove unrealistic, depending on how common the elevated N/O ratios prove to be with a larger sample. Steidel et al. (2014) on the other hand appeal to stellar population models including binaries and rotation in massive stars (e.g., Eldridge & Stanway 2009). Such stellar evolution models may be particularly appropriate for high-redshift star-forming galaxies, as argued by Steidel et al. (2014), and feature enhanced production of nitrogen by massive stars during their main sequence evolution. Stellar population synthesis models and observations of the rest-frame UV spectra of galaxies over a wide range of N/O abundance ratios will prove

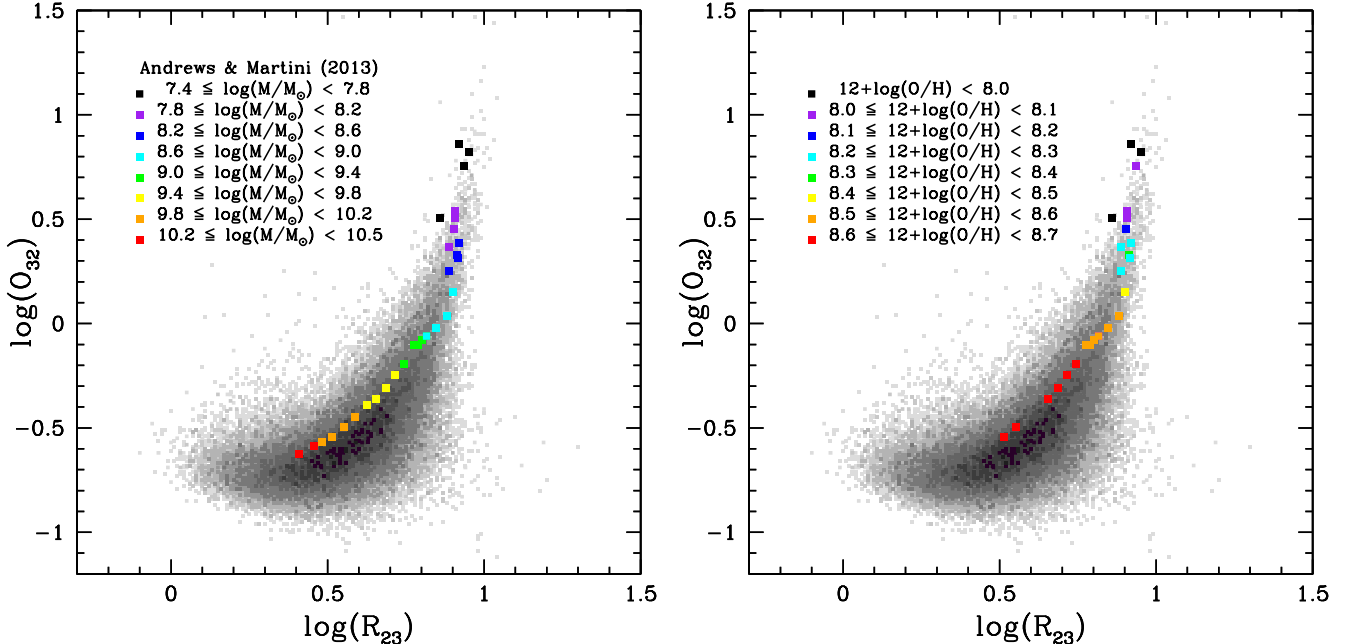


**Figure 9.** SDSS  $O_{32}$  vs.  $R_{23}$  excitation diagram, along with measurements from SDSS composite spectra from Andrews & Martini (2013) with direct oxygen abundances. In both panels, points have been corrected for dust extinction, and the larger symbols represent strong-line ratios measured from the Andrews & Martini composite spectra in bins of stellar mass. Left: The legend indicates how color corresponds to stellar mass for each composite spectrum. As in both the samples of individual SDSS and  $z \sim 2.3$  MOSDEF galaxies, the Andrews & Martini composites indicate a clear progression in stellar mass along the  $O_{32}$  vs.  $R_{23}$  excitation sequence. Right: The legend indicates how color corresponds to metallicity for each composite spectrum. The metallicity of the Andrews & Martini stacks decreases monotonically along the  $O_{32}$  vs.  $R_{23}$  sequence, as  $O_{32}$  and  $R_{23}$  increase. This smooth decline in metallicity suggests the combination of  $O_{32}$  and  $R_{23}$  as a powerful metallicity indicator, which can be calibrated to the direct oxygen abundance scale.

a promising avenue for connecting observations of rest-frame optical emission lines and high-redshift stellar populations. The rest-frame UV contains multiple features associated with stellar winds (e.g., C IV $\lambda$ 1548, 1550 P-Cygni and He II $\lambda$ 1640), and a correlation of the properties of these features with N/O will likely provide important constraints on chemical enrichment and stellar evolution in the early universe.

#### 4.2. The $O_{32}$ vs. $R_{23}$ Diagram: A Robust Abundance Indicator at High Redshift

The offset in the [OIII] $\lambda$ 5007/H $\beta$  vs. [NII] $\lambda$ 6585/H $\alpha$  BPT diagram raises concerns about estimating metallicities at high redshift from strong-line methods that include nitrogen features (e.g., the N2 and  $O3N2$  indicators; Pettini & Pagel 2004). Various authors have attempted to quantify the bias in applying the locally-calibrated N2 and  $O3N2$  indicators to high-redshift samples that follow different distributions in the [OIII] $\lambda$ 5007/H $\beta$  vs. [NII] $\lambda$ 6585/H $\alpha$  BPT diagram (Liu et al. 2008; Newman et al. 2014; Steidel et al. 2014). Both Liu et al. (2008) and Newman et al. (2014) conclude that the N2 indicator will overestimate gas-phase oxygen abundances for high-redshift galaxies, while Liu et al. (2008) and Steidel et al. (2014) conclude that the  $O3N2$  indicator should not be significantly biased, relative to its use in the local universe. However, this indicator still includes the [NII]/H $\alpha$  ratio, the value of which relative to oxygen abundance will depend on the N/O ratio.

In the  $O_{32}$  vs.  $R_{23}$  diagram, on the other hand, there is no observed offset between the  $z \sim 2.3$  MOSDEF sam-

ple and local galaxies. Furthermore, the emission lines featured in this diagram consist only of oxygen and hydrogen transitions, i.e. more direct probes of the oxygen abundance, and are immune to the variations in abundance ratios that affect abundance indicators based on nitrogen lines. These factors suggest that an abundance indicator based on  $O_{32}$  and  $R_{23}$  holds much promise for tracking the evolution in oxygen abundance over cosmic time. Although the  $R_{23}$  indicator has commonly been used to estimate oxygen abundances, Steidel et al. (2014) points out that it is of limited sensitivity over the range of metallicities spanned by the majority of high-redshift galaxies studied thus far (see their Figure 10). We confirm this result, in that  $\sim 90\%$  of the  $z \sim 2.3$  MOSDEF galaxies with  $R_{23}$  measurements fall within a range of only 0.4 dex in  $R_{23}$ . However, we observe a significant spread of the sample when considering the combination of  $R_{23}$  and  $O_{32}$ , in that  $O_{32}$  increases over a range of  $\sim 1.5$  dex as  $R_{23}$  increases by  $\sim 0.5$  dex. This same trend is traced out with much more significance in the SDSS sample, where the full sequence in  $O_{32}$  and  $R_{23}$  extends from a plateau of roughly constant  $\log(O_{32})$  values of  $\sim -0.7$  dex and  $\log(R_{23}) = 0.1 - 0.5$  dex, up through a correlated region where  $\log(O_{32})$  and  $\log(R_{23})$  both increase up to  $\sim 1$  dex.

The translation of this sequence to one of physical properties becomes clear as we consider the segregation along it with stellar mass. Figure 6 shows a clean segregation in the  $z \sim 2.3$  MOSDEF sample at the median stellar mass, with low-mass galaxies occupying the upper-right portion of the  $z \sim 2.3$   $O_{32}$  vs.  $R_{23}$  distribution, and high-mass galaxies the lower-left. The SDSS sample

also shows a systematic variation of mass with position along the sequence of  $O_{32}$  vs.  $R_{23}$ , with the lowest-mass systems dominating the distribution at the highest  $O_{32}$  and  $R_{23}$  values and the highest-mass galaxies dominating the plateau at low  $O_{32}$  and  $R_{23}$ . Given the strong correlation between stellar mass and oxygen abundance, this segregation by mass is a direct reflection of metallicity decreasing systematically along the  $O_{32}$  vs  $R_{23}$  sequence, as we traverse from the high-mass, low  $O_{32}$  and  $R_{23}$  regime into the one of the low-mass, high  $O_{32}$  and  $R_{23}$ .

Figure 6 (right) in fact reflects the well-known evolution in the mass-metallicity relation (MZR) observed between  $z \sim 0$  and  $z \sim 2$  (e.g., Erb et al. 2006a; Sanders et al. 2014; Steidel et al. 2014). Accordingly, at fixed stellar mass, galaxies appear to evolve by somewhere between  $\sim 0.15$  and  $0.3$  dex towards lower metallicities (though the exact evolution inferred depends on how metallicities are estimated and the high-redshift sample used for comparison with SDSS). This evolution can also be cast in terms of galaxies of fixed metallicity corresponding to lower-mass galaxies in the local universe than at high redshift. The median stellar mass of the  $z \sim 2.3$  MOSDEF sample plotted in Figure 6 is  $\sim 10^{10} M_{\odot}$ , while the median stellar mass of the SDSS galaxies occupying the same portion of the  $O_{32}$  vs.  $R_{23}$  diagram is  $\sim 10^9 M_{\odot}$ . Alternatively, when we construct an SDSS sample matched in median stellar mass to the  $z \sim 2.3$  MOSDEF sample, we find that it is offset towards lower  $O_{32}$  and  $R_{23}$  values relative to the  $z \sim 2.3$  MOSDEF sample. These two results follow directly if location along the sequence of  $O_{32}$  vs.  $R_{23}$  corresponds closely to oxygen abundance.

We use the composite spectra of Andrews & Martini (2013) to demonstrate the utility of the  $O_{32}$  vs.  $R_{23}$  diagram as a metallicity indicator. Andrews & Martini (2013) constructed composite spectra for SDSS galaxies in bins of stellar mass, and used measurements of auroral [OII] and [OIII] emission lines to estimate both electron temperatures and “direct” oxygen abundances as a function of stellar mass. Such estimates of  $12 + \log(\text{O}/\text{H})$  are completely independent of the strong-line methods commonly used to determine metallicity, and therefore offer a powerful empirical probe of the connection between metallicity and the observed patterns of strong emission lines. In Figure 9 (left), we show a clear progression in stellar mass among the Andrews & Martini composite spectra along the  $O_{32}$  vs.  $R_{23}$  sequence. Again, lower-mass composites in the Andrews & Martini sample occupy the upper right portion of the  $O_{32}$  vs.  $R_{23}$  sequence, while the higher-mass composites curve down and to the left. Since the majority of stellar mass composites from Andrews & Martini (2013) have direct oxygen abundances, we can also examine how direct oxygen abundance varies as a function of location along the sequence of  $O_{32}$  vs.  $R_{23}$ . Figure 9 (right) shows that there is a basically monotonic decrease in metallicity along the  $O_{32}$  vs.  $R_{23}$  sequence, extending from the lower left to upper right. This clean variation of direct oxygen abundance with location in the  $O_{32}$  vs.  $R_{23}$  diagram suggests an extremely promising metallicity indicator. Given that the  $z \sim 2.3$  MOSDEF sample follows the same distribution as SDSS galaxies in  $O_{32}$  vs.  $R_{23}$ , a calibration of oxygen abundance with  $O_{32}$  vs.  $R_{23}$  location based on

SDSS should also work for  $z \sim 2$ .

The  $O_{32}$  vs.  $R_{23}$  diagram has long been known as a probe of both ionization parameter and metallicity (Kewley & Dopita 2002), and has even been used to estimate oxygen abundances at  $z \sim 2$  (Nakajima et al. 2013; Nakajima & Ouchi 2014). In fact, just as we discuss above, Nakajima et al. (2013) also point out the fact that low-mass, low-metallicity SDSS galaxies occupy the same region of  $O_{32}$  vs.  $R_{23}$  parameter space as high-redshift galaxies. However, in both Kewley & Dopita (2002) and Nakajima et al. (2013), the combination of  $O_{32}$  and  $R_{23}$  is translated to a combination of metallicity and ionization parameter using the results of photoionization models. In contrast, here we propose to estimate oxygen abundances with an empirical calibration of  $O_{32}$  and  $R_{23}$  values based on direct oxygen abundances (Shapley et al., in prep). This  $O_{32}R_{23}$  abundance indicator will be tied to the abundance scale of the direct oxygen abundances and applicable out to at least  $z \sim 2$ , given the apparent lack of evolution in the  $O_{32}$  vs.  $R_{23}$  sequence over this interval. Accordingly, it will be possible to infer metallicities in an unbiased fashion over a wide range of redshifts with the measurement of dust-corrected [OII] $\lambda\lambda 3726, 3729$ , H $\beta$ , and [OIII] $\lambda 5007$  emission fluxes. Dust corrections ideally would be obtained using measurements of the Balmer decrement from the H $\alpha$ /H $\beta$  ratio (Reddy et al., in prep.), but may also be estimated from stellar population modeling, with the assumption of how nebular and stellar extinctions are related (e.g., Erb et al. 2006b; Förster Schreiber et al. 2009; Steidel et al. 2014).

The simultaneous detection of [OII] $\lambda\lambda 3726, 3729$ , H $\beta$ , [OIII] $\lambda 5007$ , and H $\alpha$  emission lines is becoming feasible at  $z > 1$  with the current generation of multi-object near-IR spectrographs. However, given that most high-redshift datasets are still based on more limited sets of rest-frame optical emission lines, it will be important to determine the translations between oxygen abundances based on commonly-used indicators such as  $N2$  and  $O3N2$ , and the directly-calibrated  $O_{32}R_{23}$  indicator proposed here. Such translations would be analogous to those proposed by Kewley & Ellison (2008) for the local universe, but appropriate for higher-redshift samples with different footprints in the [OIII]/H $\beta$  vs. [NII]/H $\alpha$  BPT diagram (see Sanders et al. 2014; Steidel et al. 2014, for a discussion of how the translation between the  $N2$  and  $O3N2$  indicators evolves with redshift).

With unbiased oxygen abundance measurements in hand, it will be possible to determine the evolution of the shape and normalization of the MZR in a robust fashion over at least 10 Gyr, with important implications for understanding the nature of gas flows in galaxies (Finlator & Davé 2008; Davé et al. 2011, 2012). We must also understand the origins of the differences in N/O abundance ratios at high redshift as well as characterize the physical conditions in high-redshift star-forming regions. The rich dataset of the MOSDEF survey will enable such investigations in an unprecedented manner.

We thank the referee for an extremely constructive report. We acknowledge support from NSF AAG grants AST-1312780, 1312547, 1312764, and 1313171 and grant

AR-13907 from the Space Telescope Science Institute. We are also grateful to Marc Kassis at the Keck Observatory for his many valuable contributions to the execution of the MOSDEF survey. We also acknowledge the 3D-HST collaboration, who provided us with spectroscopic and photometric catalogs used to select MOSDEF targets and derive stellar population parameters. We thank I. McLean, K. Kulas, and G. Mace for taking observations for the MOSDEF survey in May and June 2013. MK acknowledges support from a Committee Faculty Research Grant and a Hellman Fellowship. ALC acknowledges funding from NSF CAREER grant AST-1055081. NAR is supported by an Alfred P. Sloan Research Fellowship. We wish to extend special thanks to those of Hawaiian ancestry on whose sacred mountain we are privileged to be guests. Without their generous hospitality, most of the observations presented herein would not have been possible.

## REFERENCES

- Abazajian, K. N., Adelman-McCarthy, J. K., Agüeros, M. A., et al. 2009, *ApJS*, 182, 543
- Andrews, B. H., & Martini, P. 2013, *ApJ*, 765, 140
- Baldwin, J. A., Phillips, M. M., & Terlevich, R. 1981, *PASP*, 93, 5
- Brammer, G. B., van Dokkum, P. G., Franx, M., et al. 2012, *ApJS*, 200, 13
- Brinchmann, J., Pettini, M., & Charlot, S. 2008, *MNRAS*, 385, 769
- Calzetti, D., Armus, L., Bohlin, R. C., et al. 2000, *ApJ*, 533, 682
- Cardelli, J. A., Clayton, G. C., & Mathis, J. S. 1989, *ApJ*, 345, 245
- Chabrier, G. 2003, *PASP*, 115, 763
- Coil, A. L., Aird, J., Reddy, N. A., et al. 2014, *ArXiv e-prints*, arXiv:1409.6522
- Conroy, C., Gunn, J. E., & White, M. 2009, *ApJ*, 699, 486
- Davé, R., Finlator, K., & Oppenheimer, B. D. 2011, *MNRAS*, 416, 1354
- . 2012, *MNRAS*, 421, 98
- Domínguez, A., Siana, B., Henry, A. L., et al. 2013, *ApJ*, 763, 145
- Dopita, M. A., Sutherland, R. S., Nicholls, D. C., Kewley, L. J., & Vogt, F. P. A. 2013, *ApJS*, 208, 10
- Eldridge, J. J., & Stanway, E. R. 2009, *MNRAS*, 400, 1019
- Erb, D. K., Shapley, A. E., Pettini, M., et al. 2006a, *ApJ*, 644, 813
- Erb, D. K., Steidel, C. C., Shapley, A. E., et al. 2006b, *ApJ*, 647, 128
- Ferland, G. J., Korista, K. T., Verner, D. A., et al. 1998, *PASP*, 110, 761
- Finlator, K., & Davé, R. 2008, *MNRAS*, 385, 2181
- Förster Schreiber, N. M., Genzel, R., Bouché, N., et al. 2009, *ApJ*, 706, 1364
- Grogin, N. A., Kocevski, D. D., Faber, S. M., et al. 2011, *ApJS*, 197, 35
- Hainline, K. N., Shapley, A. E., Kornei, K. A., et al. 2009, *ApJ*, 701, 52
- Juneau, S., Bournaud, F., Charlot, S., et al. 2014, *ApJ*, 788, 88
- Kauffmann, G., Heckman, T. M., Tremonti, C., et al. 2003, *MNRAS*, 346, 1055
- Kennicutt, R. C. 1998, *ARA&A*, 36, 189
- Kewley, L. J., & Dopita, M. A. 2002, *ApJS*, 142, 35
- Kewley, L. J., Dopita, M. A., Leitherer, C., et al. 2013, *ApJ*, 774, 100
- Kewley, L. J., Dopita, M. A., Sutherland, R. S., Heisler, C. A., & Trevena, J. 2001, *ApJ*, 556, 121
- Kewley, L. J., & Ellison, S. L. 2008, *ApJ*, 681, 1183
- Koekemoer, A. M., Faber, S. M., Ferguson, H. C., et al. 2011, *ApJS*, 197, 36
- Kriek, M., van Dokkum, P. G., Labbé, I., et al. 2009, *ApJ*, 700, 221
- Kriek, M., Shapley, A. E., Reddy, N. A., et al. 2014, *ArXiv e-prints*, arXiv:1412.1835
- Lilly, S. J., Carollo, C. M., & Stockton, A. N. 2003, *ApJ*, 597, 730
- Liu, X., Shapley, A. E., Coil, A. L., Brinchmann, J., & Ma, C.-P. 2008, *ApJ*, 678, 758
- Maiolino, R., Nagao, T., Grazian, A., et al. 2008, *A&A*, 488, 463
- Masters, D., McCarthy, P., Siana, B., et al. 2014, *ApJ*, 785, 153
- McLean, I. S., Steidel, C. C., Epps, H. W., et al. 2012, in *Society of Photo-Optical Instrumentation Engineers (SPIE) Conference Series*, Vol. 8446, *Society of Photo-Optical Instrumentation Engineers (SPIE) Conference Series*
- Nagao, T., Maiolino, R., & Marconi, A. 2006, *A&A*, 459, 85
- Nakajima, K., & Ouchi, M. 2014, *MNRAS*, 442, 900
- Nakajima, K., Ouchi, M., Shimasaku, K., et al. 2013, *ApJ*, 769, 3
- Newman, S. F., Buschkamp, P., Genzel, R., et al. 2014, *ApJ*, 781, 21
- Osterbrock, D. E. 1989, *Astrophysics of gaseous nebulae and active galactic nuclei*
- Pérez-Montero, E., & Contini, T. 2009, *MNRAS*, 398, 949
- Pettini, M., & Pagel, B. E. J. 2004, *MNRAS*, 348, L59
- Price, S. H., Kriek, M., Brammer, G. B., et al. 2014, *ApJ*, 788, 86
- Sanders, R. L., Shapley, A. E., Kriek, M., et al. 2014, *ArXiv e-prints*, arXiv:1408.2521
- Sérsic, J. L. 1968, *Atlas de galaxias australes*
- Shapley, A. E., Coil, A. L., Ma, C.-P., & Bundy, K. 2005, *ApJ*, 635, 1006
- Shapley, A. E., Steidel, C. C., Pettini, M., & Adelberger, K. L. 2003, *ApJ*, 588, 65
- Shirazi, M., Brinchmann, J., & Rahmati, A. 2014, *ApJ*, 787, 120
- Skelton, R. E., Whitaker, K. E., Momcheva, I. G., et al. 2014, *ArXiv e-prints*, arXiv:1403.3689
- Steidel, C. C., Rudie, G. C., Strom, A. L., et al. 2014, *ArXiv e-prints*, arXiv:1405.5473
- Storey, P. J., & Zeppen, C. J. 2000, *MNRAS*, 312, 813
- Tremonti, C. A., Heckman, T. M., Kauffmann, G., et al. 2004, *ApJ*, 613, 898
- Veilleux, S., & Osterbrock, D. E. 1987, *ApJS*, 63, 295
- Verdolini, S., Yeh, S. C. C., Krumholz, M. R., Matzner, C. D., & Tielens, A. G. G. M. 2013, *ApJ*, 769, 12
- Wright, S. A., Larkin, J. E., Graham, J. R., & Ma, C.-P. 2010, *ApJ*, 711, 1291
- Yeh, S. C. C., Verdolini, S., Krumholz, M. R., Matzner, C. D., & Tielens, A. G. G. M. 2013, *ApJ*, 769, 11
- York, D. G., Adelman, J., Anderson, Jr., J. E., et al. 2000, *AJ*, 120, 1579